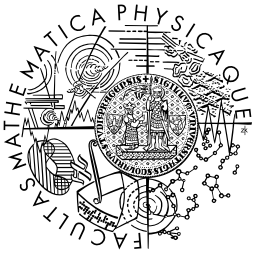

MATEMATICKO-FYZIKÁLNÍ FAKULTA
Univerzita Karlova

BAKALÁŘSKÁ PRÁCE

Michal Krištof

Detekce fotonů s pomocí plynových elektronových násobičů v čerenkovských detektorech

Katedra fyziky nízkých teplot

Vedoucí bakalářské práce: Michael Finger, M.Sc., CSc.

Studijní program: Physics

Studijní obor: General Physics

Praha 2016

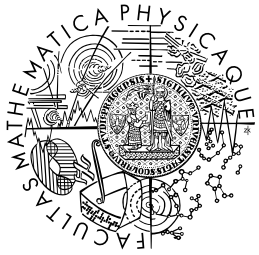

FACULTY
OF MATHEMATICS
AND PHYSICS
Charles University

BACHELOR THESIS

Michal Krištof

Gas electron multiplier based photon detection for Cherenkov imaging applications

Department of Low-Temperature Physics

Supervisor of the bachelor thesis: Michael Finger, M.Sc., CSc.

Study programme: Physics

Study branch: General Physics

Prague 2016

I declare that I carried out this bachelor thesis independently, and only with the cited sources, literature and other professional sources.

I understand that my work relates to the rights and obligations under the Act No. 121/2000 Sb., the Copyright Act, as amended, in particular the fact that the Charles University in Prague has the right to conclude a license agreement on the use of this work as a school work pursuant to Section 60 subsection 1 of the Copyright Act.

In ..... date ..... signature of the author

Název práce: Detekce fotonů s pomocí plynových elektronových násobičů v čerenkovských detektorech

Autor: Michal Krištof

Katedra: Katedra fyziky nízkých teplot

Vedoucí bakalářské práce: Michael Finger, M.Sc., CSc., Katedra fyziky nízkých teplot

Abstrakt: V práci se zabýváme popisem metod užívaných k detekci fotonů v Ring Imaging Cherenkov detektorech a základním principem jejich fungování. Předkládáme popis základních principů funkce plynových detektorů a zabýváme se vývojem nového systému detekce fotonů pro detektor RICH-1 na experimentu COMPASS založeného na Thick GEM detektorech, popisujeme jak detailně nejnovější testy oněch detektorů, tak spletitou cestu vývoje detektorů založených na ThGEM technologii. Hodnotíme výkonnost detektorů na bázi ThGEM technologie v porovnání s jinými metodami užívanými k detekci fotonů.

Klíčová slova: RICH detector Particle identification THGEM detector

Title: Gas electron multiplier based photon detection for Cherenkov imaging applications

Author: Michal Krištof

Department: Department of Low-Temperature Physics

Supervisor: Michael Finger, M.Sc., CSc., Department of Low-Temperature Physics

Abstract: In the thesis we focus on the methods used to detect photons in Ring Imaging Cherenkov detectors, their description and the basics of the physical phenomena which lie behind them. We provide a brief description of the gaseous detector types and we describe the development of the new Thick GEM based detection system for the RICH-1 of the COMPASS experiment. We provide a detailed description of the latest tests and the convoluted route of the research done in the field. We review the ThGEM-based detector performance in comparison to the other methods of detection.

Keywords: RICH detector Particle identification THGEM detector

I would like to express my humblest gratitude to my supervisor, dr. Finger, for his guidance and to prof. Finger for the possibility to work at the COMPASS experiment and also to the team of RICH people from INFN, namely Fulvio Tessarotto, Stefano Levorato, Shuddha Dasgupta and others. I would also like to express a special thanks to the Hungarian scientists of ALICE experiment for the skills and knowledge they have taught me, especially to Gergoe Hamar and Gabor Kiss and also to my colleagues from the Joint Czech Group at CERN, M. Bodlák, M. Roskot, M. Pešek, M. Pešková, J. Matoušek and M. Slunéčka for their help and company.

Contents

Introduction

The CERN, European Center for Nuclear Research, has played a major role in the physics research for more than 60 years, providing an insight to the physics of elementary particles. It was established on the initiative of the leading European scientists by the European Council for Nuclear Research after the second world war. It is a collaboration of mainly European nations on a common scientific goal.

To the most spectacular and also the most widely known contributions of this organization to the general physical knowledge belongs also the historical breakthrough in science awarded by the Nobel Prize in Physics, the discovery of the Higgs Boson[1].

This organization comprises of thousands of researchers working on different experiments, however, in its roots, all of the experiments have a single detail in common, and it is the need of the particle identification(PID) system. In this thesis, we will be focusing on one of the systems used, the particle identification using the principle of detecting the Cherenkov radiation, used in this particular case on the COMPASS experiment in CERN and on the research and development of a new detection apparatus for this particular experiment.

The COMPASS experiment, is a particle physics experiment designed to study the structure and spectroscopy of hadron particles. To achieve this, it exploits high intensity muon and hadron beams extracted form the Super Proton Synchrotron accelerator and shot into a fixed target. Particles produced in the interaction of the beam with the target are recorded by a set of detectors. A vital component of a particle identification system in this experiment used to distinguish charged hadrons is the RICH-1 Ring Imaging Cherenkov counter[2].

RICH counters are a powerful tool for particle identification[12] since their conception in 1970's. They were and are a part of a vast portion of experiments in the field of particle physics, the most prominent being ALICE, LHCb(CERN), BaBar-DIRC(SLAC) and AMS(ISS)[27]. For this reason the development of this scientific apparatus is essential in not only COMPASS experiment, but also for many other present and future experiments.

1. The Vavilov-Cherenkov effect and the basis for the RICH counter measurement

The Vavilov-Cherenkov(VC) effect is a physical phenomenon occurring when a charged particle moves in a medium with a velocity greater than the phase velocity of light in that medium. It is an effect analogous to the Mach effect, a physical phenomenon arising when an aircraft or a bullet travels through the air at supersonic speed. In that case, a conical shock-wave is created with its apex at the position of the moving body[15].

Although it is bearing the name of two of the most prominent soviet scientists of the first half of the 20th century, it was actually theorized long before its first experimental description. It was described by Oliver Heaviside in 1889, however, his works were forgotten[40].

We can also find some observational notices of a blue light in radioactive or irradiated solutions before the experimental description of Cherenkov. In years 1900-1905, a blue light was reportedly observed by the Curies coming out of radium solutions, however, this observation was left uninterpreted. The second observational notice comes from the year of 1926, when a french physicist M.L. Mallet published a work describing a specific radiation observed in water irradiated by gamma rays, however, in this work he interprets this phenomenon as luminescence[32].

The VC effect was discovered experimentally and properly described by Pavel Alexeevich Cherenkov in his experiments, which he conducted in the years of 1934-1937 for his dissertation thesis. These experiments were performed at the suggestion of his teacher S.I. Vavilov. Cherenkov used a radioactive source to emit gamma photons into a bottle of water with an interesting result. In the water, the photons induced a blue light, which he associated to the electrons torn from the water molecules via the Compton scattering by the incoming gamma photons.

At first, Cherenkov, together with Vavilov, assumed, that the blue light is caused by the deceleration of the Compton electrons, since the electrons were fully absorbed in the water. However in the year 1937 he changed his opinion in favour of Tamm-Frank theory. Tamm and Frank were theoretical physicists, who studied electrodynamic effects of a charge uniformly moving through a medium. They published a paper in 1937, results of which were in agreement with the experiments conducted by Cherenkov.

The physical principle behind this phenomenon is of an electrodynamic basis. The electric field of a moving charge induces a time-dependent polarization in the material. This polarization oscillates and these oscillations of polarization, being added, lead to the appearance of Cherenkov cones[15].

These experiments conducted in 1934-1937 have gained Cherenkov together with Tamm and Frank a Nobel Prize in Physics in 1958[6].

1.1 Uniform motion of a charged particle in a medium

To show that a particle moving in a medium produces the Cherenkov radiation, we first need to calculate an electromagnetic field generated by this particle. For this, we will consider a point-like particle moving along the trajectory of $\vec{\xi}(t')$ in an infinite medium and characterize its charge density ρ as the Dirac delta function multiplied by the charge of the particle q and its current density $\vec{J}$ as the Dirac delta function multiplied by the speed of the particle $\vec{v}$ and its charge[33].

This situation is an approximation as we are often dealing with finite regions of space and dispersive media. In the end of this chapter we will see that this situation is a simple example providing a good demonstration that leads to creation of electromagnetic field representing a simple Cherenkov shock wave.

We will need to define the time of the irradiation, t', and the time of the detection t, for which must hold[15]

$$c_n(t-t') = |\vec{r} - \vec{\xi}(t')|, \tag{1.1}$$

where $\vec{r}$ is the position of the observer and c_n is the speed of light in the medium(as opposed to c, the speed of light in a vacuum).

Now we are able to formulate the charge and current densities.

$$\rho(\vec{r}', t') = q\delta^3(\vec{r}' - \vec{\xi}(t')),\ \vec{J}(\vec{r}', t') = q\vec{v}(t')\delta^3(\vec{r}' - \vec{\xi}(t')) \tag{1.2}$$

And to find the vector and scalar potentials $\vec{A}$ and ϕ.

$$\begin{aligned} \phi(\vec{r}, t) &= \frac{1}{4\pi\epsilon_0}\int_{\mathbb{R}^3}\frac{\rho(\vec{r}', t')}{|\vec{r} - \vec{r}'|}\mathrm{d}^3\vec{r}' = \frac{1}{4\pi\epsilon_0}\int_{\mathbb{R}^3}\frac{q\delta^3(\vec{r}' - \vec{\xi}(t'))}{|\vec{r} - \vec{r}'|}\mathrm{d}^3\vec{r}' \\ \vec{A}(\vec{r}, t) &= \frac{\mu_0}{4\pi}\int_{\mathbb{R}^3}\frac{\vec{J}(\vec{r}', t')}{|\vec{r} - \vec{r}'|}d^3\vec{r}' = \frac{\mu_0}{4\pi}\int_{\mathbb{R}^3}\frac{q\vec{v}(t')\delta^3(\vec{r}' - \vec{\xi}(t'))}{|\vec{r} - \vec{r}'|}d^3\vec{r}' \end{aligned} \tag{1.3}$$

To evaluate these integrals, we need to use a trick. This trick consists of rewriting the integral using yet another δ-function, but this time in time(using the fact, that $\int_{-\infty}^{\infty} f(\xi)\delta(\xi - x)\mathrm{d}\xi = f(x)$).

$$\begin{aligned} \phi(\vec{r}, t) &= \frac{1}{4\pi\epsilon_0}\int_{\mathbb{R}^3}\int_{-\infty}^{\infty}\frac{q\delta^3(\vec{r}' - \vec{\xi}(\tau))}{|\vec{r} - \vec{r}'|}\delta(\tau - t')\mathrm{d}\tau\mathrm{d}^3\vec{r}' \\ \vec{A}(\vec{r}, t) &= \frac{\mu_0}{4\pi}\int_{\mathbb{R}^3}\int_{-\infty}^{\infty}\frac{q\vec{v}(\tau)\delta^3(\vec{r}' - \vec{\xi}(\tau))}{|\vec{r} - \vec{r}'|}\delta(\tau - t')\mathrm{d}\tau\mathrm{d}^3\vec{r}' \end{aligned} \tag{1.4}$$

By exchanging the order of integration we can integrate the spatial integral and get

$$\begin{aligned} \phi(\vec{r}, t) &= \frac{1}{4\pi\epsilon_0}\int_{-\infty}^{\infty}\frac{q\delta(\tau - t')}{|\vec{r} - \vec{\xi}|}\mathrm{d}\tau \\ \vec{A}(\vec{r}, t) &= \frac{\mu_0}{4\pi}\int_{-\infty}^{\infty}\frac{q\vec{v}(\tau)\delta(\tau - t')}{|\vec{r} - \vec{\xi}|}\mathrm{d}\tau \end{aligned} \tag{1.5}$$

By using the identity[26]

$$\delta(f(x)) = \sum_{i=1}^{n}\frac{\delta(x - a_i)}{|f'(a_i)|} \tag{1.6}$$

where a_i is the zero point of $f(x)$, where we use the equation (1.1), from which $t' = t'(t, \vec{r})$. We set $x := \tau$ and $f(\tau) := \tau - t'$:

$$\delta(\tau - t') = \sum_{t_i} \frac{\delta(\tau - t_i)}{\frac{\partial}{\partial \tau}\left(\tau - \left(t - \frac{1}{c_n}|\vec{r} - \vec{\xi}(\tau)|\right)\right)\Big|_{\tau=t_i}} \tag{1.7}$$

where t_i are roots of equation (1.1).

By labeling $\vec{v}_i := \vec{v}(t_i) = \frac{\mathrm{d}\xi}{\mathrm{d}\tau}|_{\tau=t_i}$, we get the Liénard-Wiechert potentials

$$\begin{aligned} \phi(\vec{r}, t) &= \frac{1}{4\pi\epsilon_0} \sum_{t_i} \frac{q}{||\vec{r} - \vec{\xi}(t_i)| - \vec{v}_i(\vec{r} - \vec{\xi}(t_i))/c_n|} \\ \vec{A}(\vec{r}, t) &= \frac{\mu_0}{4\pi} \sum_{t_i} \frac{q\vec{v}_i}{||\vec{r} - \vec{\xi}(t_i)| - \vec{v}_i(\vec{r} - \vec{\xi}(t_i))/c_n|} \end{aligned} \tag{1.8}$$

Before we continue, let us investigate the t_i roots. Without loss of generality, let us consider particle motion in the direction of z axis. For this motion, we can express the trajectory as

$$\vec{\xi}(t) = (0, 0, vt) \tag{1.9}$$

We will start by squaring the equation 1.1 and isolating $c_n t'$.

$$-2c_n t'(tc_n - z\beta_n) + c_n^2 t'^2(1 - \beta_n^2) = x^2 + y^2 + z^2 - c_n^2 t^2 \tag{1.10}$$

where we labeled $\beta_n := v/c_n$. We will also use $\beta = v/c$ and the relation $n\beta = \beta_n$ where $n = c/c_n$.

This equation has solutions

$$c_n t' = \frac{c_n t - \beta_n z}{1 - \beta_n^2} \mp \frac{r_m}{|1 - \beta_n^2|} \tag{1.11}$$

with $r_m := \sqrt{(x^2 + y^2)(1 - \beta_n^2) + (z - vt)^2}$.

By subtracting $c_n t$ to the both sides we can also get

$$c_n(t - t') = \beta_n \frac{vt - z}{\beta_n^2 - 1} \pm \frac{r_m}{|\beta_n^2 - 1|} \tag{1.12}$$

which leads to the equation

$$c_n^2(t - t_1)(t - t_2) = \frac{(z - vt)^2 + x^2 + y^2}{\beta_n^2 - 1} \tag{1.13}$$

where we denoted the solution for positive sign in (1.12) as t_1 and for negative sign t_2.

As we can see, the (1.13) can be negative if and only if $\beta_n^2 < 1$. In this case the particle moves with a velocity $v < c_n$ and it also means, that $(t - t_1)$ is of a different sign than the $(t - t_2)$, one of which has to be positive and the other negative.

From these solutions, only the positive one is physical which means we should choose only the upper sign in (1.12) and hence also in (1.11), which gives us potentials

$$\phi(\vec{r}, t) = \frac{q}{\epsilon_0} \frac{1}{r_m},\ A_z = \frac{qv\mu_0}{cr_m} \tag{1.14}$$

which are the classic potentials that describe a field that the particle carries with itself, which means that no energy is emitted as we are dealing with a stationary field of a direct current that does not radiate energy.

The more interesting situation arises from the case of $\beta_n^2 > 1$ or $v > c_n$. In this case, $(t - t_1)$ and $(t - t_2)$ are of the same sign. This means, that the solution (1.12) is positive if

$$t > \frac{z}{v} \tag{1.15}$$

which coincides by the condition of positivity of r_m^2

$$-(x^2 + y^2)(1 - \beta_n^2) \leq (z - vt)^2 \tag{1.16}$$

lets denote $\gamma_n := 1/\sqrt{1 - \beta_n^2}$, the Lorentz factor, then the inequality transforms to

$$vt - z - \frac{\sqrt{x^2 + y^2}}{\gamma_n} \geq 0 \tag{1.17}$$

which is an inequality that describes the inside of a cone. We will call this cone the Cherenkov cone.

This gives us potentials

$$\begin{aligned} \phi(\vec{r}, t) &= \begin{cases} 2q\frac{1}{\epsilon_0 r_m}, & vt - z - \frac{\sqrt{x^2+y^2}}{\gamma_n} \geq 0 \\ 0, & \text{otherwise} \end{cases} \\ A_z(\vec{r}, t) &= \begin{cases} 2q\mu_0\frac{v}{c r_m}, & vt - z - \frac{\sqrt{x^2+y^2}}{\gamma_n} \geq 0 \\ 0, & \text{otherwise} \end{cases} \end{aligned} \tag{1.18}$$

in which we can clearly see that the potentials are nonzero only in the region inside of the Cherenkov cones, on the surface of the Cherenkov cones we see a divergence of potentials. We will regard to propagation of these fields as the Cherenkov shock wave.

From the relations between potentials and electric and magnetic intensities, inductions respectively

$$\vec{D} = \epsilon\vec{E} = -\epsilon\nabla\phi - \frac{\epsilon}{c}\dot{A},\ \vec{B} = \mu\vec{H} = \nabla \times \vec{A} \tag{1.19}$$

where ϵ is the permittivity and μ permeability of the medium. Rewriting the computed expressions (1.20) using the distribution language, in this case with the Heaviside step function so that we can differentiate the obtained potentials, we can compute the electromagnetic field quantities

$$\begin{aligned} H_\varphi &= -\frac{2q\rho\beta}{\gamma_n^2 r_m^3}\theta(vt - z - \rho/\gamma_n) + \frac{2q\beta}{\gamma_n r_m}\delta(vt - z - \rho/\gamma_n) \\ \vec{E} &= -\frac{2qr}{\gamma_n^2 r_m^3}\theta(vt - z - \rho/\gamma_n)\vec{n}_r + \frac{2q\beta}{\gamma_n r_m}\delta(vt - z - \rho/\gamma_n)\vec{n}_m \end{aligned} \tag{1.20}$$

where $\vec{n}_r$ is the unit radial vector directed into the Cherenkov cone from the charge current position, φ is the azimuthal coordinate on the surface of the cone, $\vec{n}_m = \vec{n}_\rho/\beta_n - \vec{n}_z/(\beta_n\gamma_n)$ is the unit vector lying on the surface of the Cherenkov cone(see Fig. 1.1), $\theta(x)$ is the Heaviside step function and $\rho = \sqrt{x^2 + y^2}$.

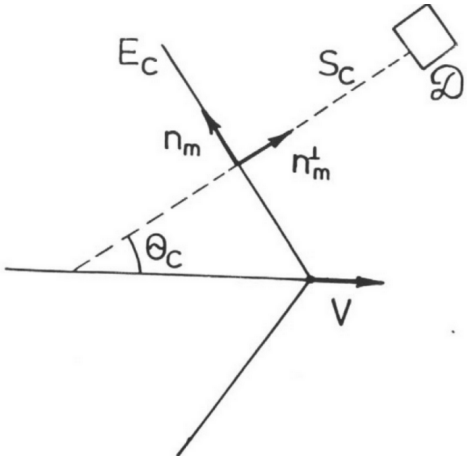

Figure 1.1: The visualization of the Cherenkov cone with $\vec{n}_m$ unit vector in (1.20) and $\vec{n}_m^{\perp}$ unit vector in (1.21). The $\mathscr{D}$ marks a detector, E_c the direction of the electric intensity, $\vec{v}$ the speed of propagation of the cone and S_c the Cherenkov photon trajectory[15].

As the r_m approaches infinity, we can omit the first term in the H_φ and $\vec{E}$ in (1.20), as it approaches zero considerably faster than the second term of (1.20) and calculate the Poynting vector in a large distance from the particle as

$$\vec{S} = \frac{c}{4\pi}\vec{E} \times \vec{H} = \frac{c}{4\pi}\sqrt{\frac{\mu_0}{\epsilon_0}}\left(\frac{2q\beta}{r_m\gamma_n}\delta(vt - z - \rho/\gamma_n)\right)^2 \vec{n}_m^{\perp} \tag{1.21}$$

where $\vec{n}_m^{\perp}$ is the unit vector normal to the surface of the Cherenkov cone.

So an observer placed at the ρ, z point will detect the Cherenkov shock wave in time $t = (z - \rho/\gamma_n)/v$. The Poynting vector hints that a shock wave created in this case, as opposed to the case of $v < c_n$, radiates energy into its surroundings[15].

1.2 The Tamm formula

Now we are going to consider a more realistic problem. Lets assume a finite interval $(-z_0, z_0)$ on the z axis, where we localize our point charge. Lets assume that in the time $-t_0$ the charge starts moving uniformly through the medium with $v > c_n$ until it reaches the endpoint of its trajectory z_0 in t_0. This is the original problem that Tamm considered in his theory. We will describe his solution of this problem.

We will solve this problem in the spectral representation using the Fourier transform of the z-component of the current density

$$j_{z,\omega} = \frac{1}{2\pi}\int_{-\infty}^{\infty} j(t)e^{-i\omega t}\mathrm{d}t \tag{1.22}$$

Lets set $R' := \sqrt{(x-x')^2 + (y-y')^2 + (z-z')^2}$. The z-component of the vector potential is then

$$A_{z,\omega} = \frac{\mu_0}{c}\int_{-\infty}^{\infty}\int_{-\infty}^{\infty}\int_{-\infty}^{\infty}\frac{j_{z,\omega}(x',y',z')}{R'}e^{-in\omega R'/c}\mathrm{d}x'\mathrm{d}y'\mathrm{d}z' \tag{1.23}$$

where $n = c/c_n$ is the refractive index of the medium.

Because the point charge moves in the z direction with the speed v, its charge density will act like a δ function in the x, y plane and in the z axis it will be nonzero only on the interval of $(-z_0, z_0)$, which can be described as a combination of Heaviside step functions, but will exist only in the time t in the point $z - vt$:

$$j(t) = qv\delta(x)\delta(y)\delta(z - vt)\theta(z - z_0)\theta(z + z_0) \tag{1.24}$$

or in the spectral image

$$j_{z,\omega} = qv\delta(x)\delta(y)e^{-i\omega z/v}\theta(z - z_0)\theta(z + z_0) \tag{1.25}$$

inserting (1.25) into (1.23) we get

$$A_{z,\omega} = \frac{qv\mu_0}{c}\int_{\mathbb{R}^3}\frac{\delta(x')\delta(y')e^{-i\omega z'/v}\theta(z' - z_0)\theta(z' + z_0)}{R'}e^{-\frac{in\omega R'}{c}}\mathrm{d}x'\mathrm{d}y'\mathrm{d}z' \tag{1.26}$$

$$A_{z,\omega} = \frac{qv\mu_0}{c}\int_{-z_0}^{z_0}\frac{e^{-in\frac{\omega}{c}(\frac{z'}{\beta_n}-\sqrt{\rho^2+(z-z')^2})}}{\sqrt{\rho^2+(z-z')^2}}\mathrm{d}z' \tag{1.27}$$

As with the previous problem, we want to know the solution further away from the particle, when $r >> z_0$. For this purpose, we use a Taylor expansion of $\sqrt{x^2+y^2+(z-z')^2}$ in the z coordinate. Setting $r := \sqrt{x^2+y^2+z^2}$ we get

$$\sqrt{\rho^2+(z-z')^2} = r - \frac{zz'}{r} + O(z^2) = r - z'\cos\theta + O(z^2) \tag{1.28}$$

where θ is the angle between z and r.

Inserting (1.28) into (1.27), one obtains

$$A_{z,\omega} = \frac{qv\mu_0 e^{in\frac{\omega}{c}r}}{2\pi c}\int_{-z_0}^{z_0}\frac{e^{-in\frac{\omega}{c\beta_n}z'(1+\beta_n\cos\theta)}}{r - z'\cos\theta}\mathrm{d}z' \tag{1.29}$$

The integral (1.29) is a bit tricky to tackle, since it is of the form of $\int e^{-tx}/x\mathrm{d}x$, which can not be expressed in terms of elementary functions and leads to exponential integral function[47]. To be exact, since we are dealing with a complex exponential, it can be divided into two real integrals using the Euler formula, replacing the exponential in (1.29) with a linear combination of a sine and cosine functions. Both integrals have no expressions in the terms of elementary functions. One integral leads to the sine integral function[48], the other leads to the cosine integral function[46]. So a trick is needed to compute the integral or a further approximation. We will follow the route of Tamm in [43] and neglect the difference between r and $\sqrt{\rho^2+(z-z')^2}$. Using this neglection, we get:

$$A_{z,\omega} = \frac{qv\mu_0 e^{in\frac{\omega}{c}r}}{2\pi rc}\int_{-z_0}^{z_0}e^{-in\frac{\omega}{c\beta_n}z'(1+\beta_n\cos\theta)}\mathrm{d}z' \tag{1.30}$$

which can be solved using $z_0 = vt_0$ as

$$A_{z,\omega} = \frac{q\beta\mu_0}{\pi r\omega}e^{in\frac{\omega}{c}r}\frac{\sin[\omega t_0(1-\beta_n\cos\theta)]}{1-\beta_n\cos\theta} \tag{1.31}$$

We define

$$g(\omega) := \frac{\sin[\omega t_0(1-\beta_n\cos\theta)]}{1-\beta_n\cos\theta} \tag{1.32}$$

then using (1.19), the fact that the Fourier transform turns differentiation in time to multiplication by $i\omega$ and the Lorentz gauge condition for Fourier-transformed potentials

$$\operatorname{div}\vec{A}_\omega + \frac{i\omega}{c}n^2\phi_\omega = 0 \tag{1.33}$$

we find that in this case there is no need for the computation of the scalar potential and can compute the non-zero components of $\vec{E}$ and $\vec{H}$ straight away

$$\begin{aligned} H_\varphi(\omega) &= \frac{iqn\beta\sin\theta}{\pi cr}e^{-ik_nr}g(\omega) \\ E_\theta(\omega) &= \frac{iq\mu\beta\sin\theta}{\pi cr}e^{-ik_nr}g(\omega) \end{aligned} \tag{1.34}$$

where $k_n = n\omega/c$.

To finalize our effort in this chapter we will compute the energy flux through the sphere of a radius r throughout the entire motion of the charge

$$\mathcal{E} = r^2\int S_r\mathrm{d}t\mathrm{d}\Omega = r^2\int\frac{c}{4\pi}E_\theta(t)H_\varphi(t)\mathrm{d}t\mathrm{d}\Omega \tag{1.35}$$

where the integral is over the entire solid angle and all of the time(time goes from minus infinity to infinity).

However, we only know the Fourier transform of E_θ and H_φ. That can be solved by an inverse Fourier transform

$$\begin{aligned} E_\theta(t) &= \int_{-\infty}^{\infty}E_\theta(\omega)e^{i\omega t}\mathrm{d}\omega \\ H_\varphi(t) &= \int_{-\infty}^{\infty}H_\varphi(\omega)e^{i\omega t}\mathrm{d}\omega \end{aligned} \tag{1.36}$$

Inserting (1.36) into (1.35) and using the fact, that in our case, from (1.34) one can see, that $E_\theta^*H_\varphi^* + E_\theta H_\varphi = 0$ and the identity[49]

$$\frac{1}{2\pi}\int_{-\infty}^{\infty}e^{it(\omega-\omega')}\mathrm{d}t = \delta(\omega-\omega') \tag{1.37}$$

we get

$$\begin{aligned} \mathcal{E} &= \frac{r^2c}{2\pi}\int\int\Re(E_\theta(\omega')e^{i\omega' t})\mathrm{d}\omega'\int\Re(H_\varphi(\omega)e^{i\omega t})\mathrm{d}\omega\mathrm{d}t\mathrm{d}\Omega = \\ &= \frac{r^2c}{4\pi}\int H_\varphi(\omega)E_\theta^*(\omega')e^{i(\omega-\omega')t} + H_\varphi^*(\omega)E_\theta(\omega')e^{it(\omega'-\omega)}\mathrm{d}\omega\mathrm{d}\omega'\mathrm{d}t\mathrm{d}\Omega = \\ &= \frac{r^2c}{2}\int H_\varphi(\omega)E_\theta^*(\omega) + H_\varphi^*(\omega)E_\theta(\omega)\mathrm{d}\omega\mathrm{d}\Omega = \int\frac{\mathrm{d}^2\mathcal{E}}{\mathrm{d}\omega\mathrm{d}\Omega}\mathrm{d}\omega\mathrm{d}\Omega \end{aligned} \tag{1.38}$$

(for improved readability we don't include limits of integration that should be over all of the time and frequencies and through the entire solid angle)and by substituting (1.34), we come into conclusion, that

$$\frac{\mathrm{d}^2\mathcal{E}}{\mathrm{d}\omega\mathrm{d}\Omega} = \frac{q^2\mu n\beta^2\sin^2\theta}{\pi^2c}g^2(\omega) \tag{1.39}$$

This formula is called the Tamm formula and describes the energy irradiated by the moving charge into its surroundings into unit solid angle per frequency unit.

To gain measurable results, we must make another simplification by setting a large ωt_0. In this limit

$$g^2 \to \frac{\pi k_n z_0}{\beta^2 n^2} \delta\left(\cos\theta - \frac{1}{\beta n}\right) \tag{1.40}$$

and so

$$\frac{\mathrm{d}^2\mathcal{E}}{\mathrm{d}\omega\mathrm{d}\Omega} \to \frac{q^2 \mu k_n z_0}{\pi c n}\left(1 - \frac{1}{\beta_n^2}\right)\delta\left(\cos\theta - \frac{1}{\beta n}\right) \tag{1.41}$$

which can be integrated using the definition of integration of a solid angle, the (1.6) and the fact, that the Dirac delta function has an integral equal to one, to get the formula

$$\frac{\mathrm{d}\mathcal{E}}{\mathrm{d}\omega} = L\frac{q^2}{c^2}\omega\left(1 - \frac{c^2}{v^2 n^2}\right) \tag{1.42}$$

where $L = 2z_0$ is the length of the trajectory.

This formula can be used to obtain the charge velocity in an experiment[15]. For this purpose, it will be handy to rewrite the Tamm formula into an integral form

$$\mathcal{E} = L\frac{q^2}{c^2}\int_{\beta_n > 1} \omega \mathrm{d}\omega \left(1 - \frac{1}{\beta_n^2}\right) \tag{1.43}$$

from which we can find(by substituing (1.42) for the energy per photon $E_p = hc/\lambda$[42] and then integrating over λ) that the number of photons emitted by electrons within the spectral region confined by the wave lengths λ_1 and λ_2 is equal to[30]

$$N = 2\pi Z^2 \alpha \left(\frac{L}{\lambda_1} - \frac{L}{\lambda_2}\right)\left(1 - \frac{1}{\beta_n^2}\right) \tag{1.44}$$

where $\alpha = e^2/(\hbar c)$ is the fine structure constant, e the charge of an electron, $\hbar$ reduced Planck's constant and Z is the number of electrons, $q = Ze$.
Or expressed differentially[27]

$$\frac{\partial N^2}{\partial z \partial \lambda} = \frac{2\pi\alpha Z^2}{\lambda^2}\left(1 - \frac{1}{\beta_n^2}\right) \tag{1.45}$$

1.3 Basic formulae for RICH measurement

Until now, we have been using an advanced mathematical methods to derive important formulae linked with the Cherenkov radiation. Now we use the basic trigonometry and optics to link the already calculated formulae to measurable units.

Using the basic trigonometry, realizing that the Cherenkov cone, the trajectory of the particle and the trajectory(characterized by the distance d_p travelled in the time t: $d_p = c_n t$) of the Cherenkov photon form a right triangle with hypotenuse being the trajectory of the particle characterized by its distance $d = vt$ (Figure 1.2), we can write

$$\cos\theta = \cos\theta_c = \frac{c_n t}{vt} = \frac{1}{\beta n} = \frac{1}{\beta_n} \tag{1.46}$$

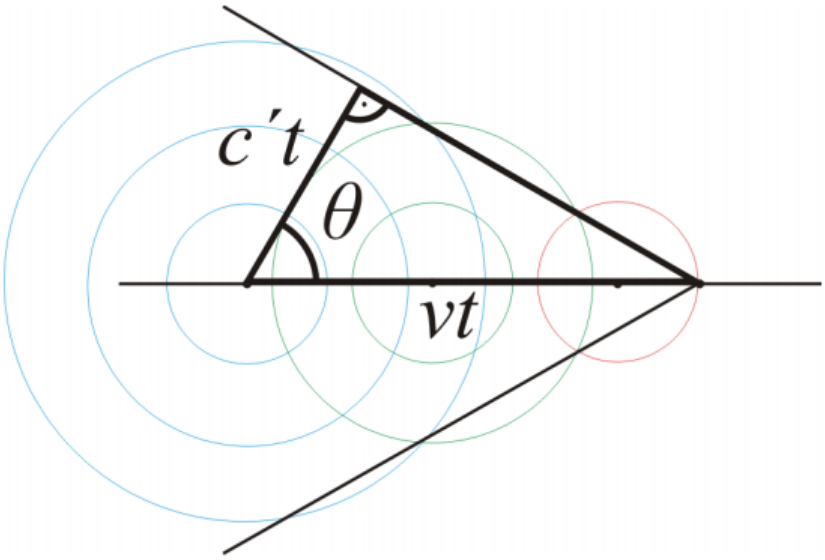

Figure 1.2: Trigonometry of the Cherenkov cone[40]. c' on this figure represents the speed of light in the medium, c_n in our marking.

where we've already introduced the subscript c to θ_c to which we will be referencing as the Cherenkov angle. More on derivation of this formula as well as description of different approaches to its derivation can be found in [40].

So we can rewrite the formula (1.45) as

$$\frac{\partial N^2}{\partial z \partial \lambda} = \frac{2\pi\alpha Z^2}{\lambda^2} \sin^2 \theta_c \tag{1.47}$$

The Cherenkov angle is important for the RICH counter measurement. The Cherenkov cone manifests itself on the detector as a ring of light. By measuring the radius of this ring, it is possible to obtain the Cherenkov angle.

For this reason it is important to mention the minimal and maximal possible measurable angle, the minimal being the angle we get by setting the velocity of the particle as the velocity threshold from which a particle emits the Cherenkov radiation, or in other words $v = c_n$

$$\beta_{\min} = \frac{v_{\min}}{c} = \frac{c_n}{c} \tag{1.48}$$

then the Cherenkov angle is

$$\cos \theta_{c,\min} = \frac{1}{\beta_{\min} n} = \frac{n}{n} = 1 \implies \theta_{c,\min} = 0 \tag{1.49}$$

And the maximal possible angle being the maximal universal speed which a particle can achieve, or the speed of light in a vacuum, $v = c$

$$\beta_{\max} = \frac{c}{c} = 1 \tag{1.50}$$

and the corresponding angle

$$\cos \theta_{c,max} = \frac{1}{n} \implies \theta_{c,max} = \arccos \frac{1}{n} \tag{1.51}$$

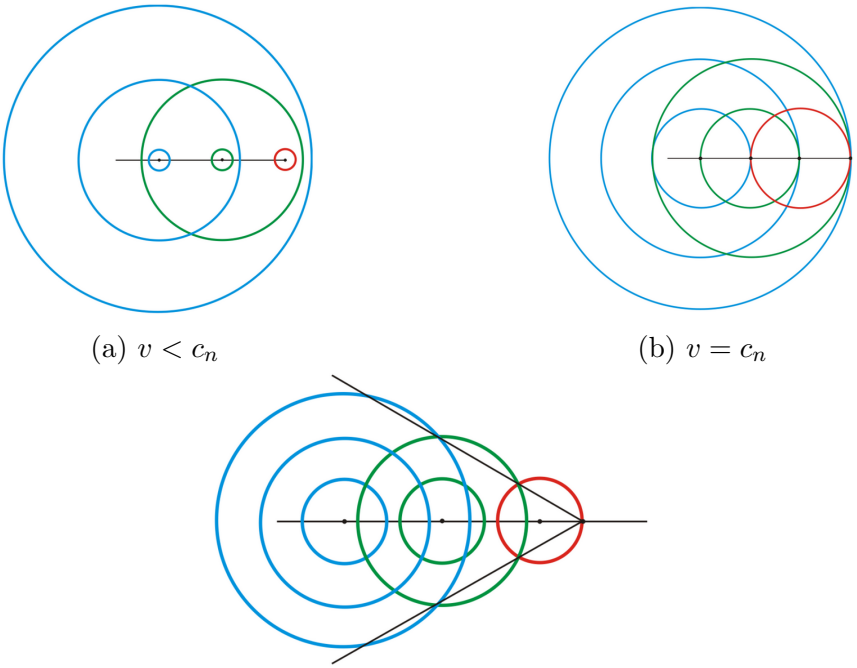

(a) $v < c_n$ (b) $v = c_n$

(c) $v > c_n$

Figure 1.3: The Cherenkov cone explanation based on the interference of light. Equiphase surfaces of a wave generated by a particle traveling with velocity v less than the speed of light in the medium c_n do not interfere (a), equiphases of a particle with $v = c$ interfere in the points of the trajectory (b) and equiphases of a particle with $v > c_n$ interfere to create the Cherenkov cone[40].

Using these thresholds, we can evaluate the measurement using a RICH counter.

Now let us focus on the actual measurement. If we are using a spherical mirror with curvature R to focus the Cherenkov ring into the detector, we apply the relation for focal length F

$$F = \frac{R}{2} \tag{1.52}$$

then the radius of the ring r on the focal surface is

$$r = F \tan\theta_c = \frac{R}{2} \tan\theta_c \tag{1.53}$$

And in small angle approximation we get

$$r \approx \frac{R}{2}\sqrt{2 - \frac{2}{n}\sqrt{1 + \frac{m^2c^2}{p^2}}} \tag{1.54}$$

where m is the mass and p momentum of the passing particle. This formula tells us, that using the RICH counter, we can either determine the speed of the particle or if the momentum of the particle is known(determined by, for example, a magnetic spectrometer), we can identify the particle by calculating its mass from the radius of the Cherenkov ring[27, 40].

2. Examples of various RICH counters used in experiments at CERN

RICH counters in general consist of two main parts - the radiator, which contains a medium in which a passing particle emits the Cherenkov radiation, and a system of detectors to detect this radiation. Different RICH counters contain different radiator materials and utilize different detection methods. Choice of the radiator material depends on the momenta of the studied particles,[35] while the choice of a detection system depends on the needs of each experiment. In this chapter we explore the different interesting designs of RICH counters used in physics experiments at CERN. This overview of different RICH counter designs demonstrates the variety of approaches to particle identification(PID) in experiments applied thanks to different experimental setups and research purposes of these experiments.

2.1 LHCb RICH-1 and RICH-2

The LHCb experiment is aimed at studying B-mesons and products of their decays. For this, it utilizes measurement in small angles from the beamline[3]. The PID system for this task makes use of two RICH counters detecting different particles in a different distances from the point of the studied interaction of particles. The PID system of LHCb comprises of three radiators, each designed to detect a different range of momenta of passing particles, with a sillica aerogel suitable for the lowest momentum tracks, the gaseous C_4F_{10} intermediate region and the gaseous CF_4 for the highest momentum region. An upstream RICH-1 contains the aerogel and C_4F_{10} radiators and a downstream RICH-2 has a CF_4 radiator. Both of these RICH counters are large scale, with the radiator dimensions of $2.4\times2.4\text{x}1\text{m}^3$ for RICH-1 and $7\times7\times2\text{m}^3$ for RICH-2. Both detectors utilize hybrid photodiodes with pixel readout. The Cherenkov light is focused to these readout units using spherical mirrors.

LHCb experiment is an interesting example of an experiment using RICH counters as method of PID and gives us glimpse to two different possible arrangements of the mirror focusing system and readout electronics.

The experimental setup can be seen on the figure 2.1. As can be seen on the figure 2.1a, the RICH-1 focusing system comprises of two spherical mirrors focused to reflect light to the detection Pixel Hybrid Photon Detectors(HPDs) located on the detector wall opposite to the mirrors. The Pixel HPDs performance resides at gains(current amplification) of 3000-5000. The mirrors have a focal length of $f = 850\,\text{mm}$, they are segmented into four $900\times750\,\text{mm}^2$ quadrants, each of which is composed of 2×2 rectangular mirror segments of $450\times750\,\text{mm}^2$. The axes of the mirror quadrants are tilted with respect to the beam axis by 286 mrad horizontally and 65 mrad vertically. Individual mirrors are made of polished glass, 6 mm in thickness, coated by vacuum deposition with 900 nm of aluminium and over-coated with 200 nm of quartz.

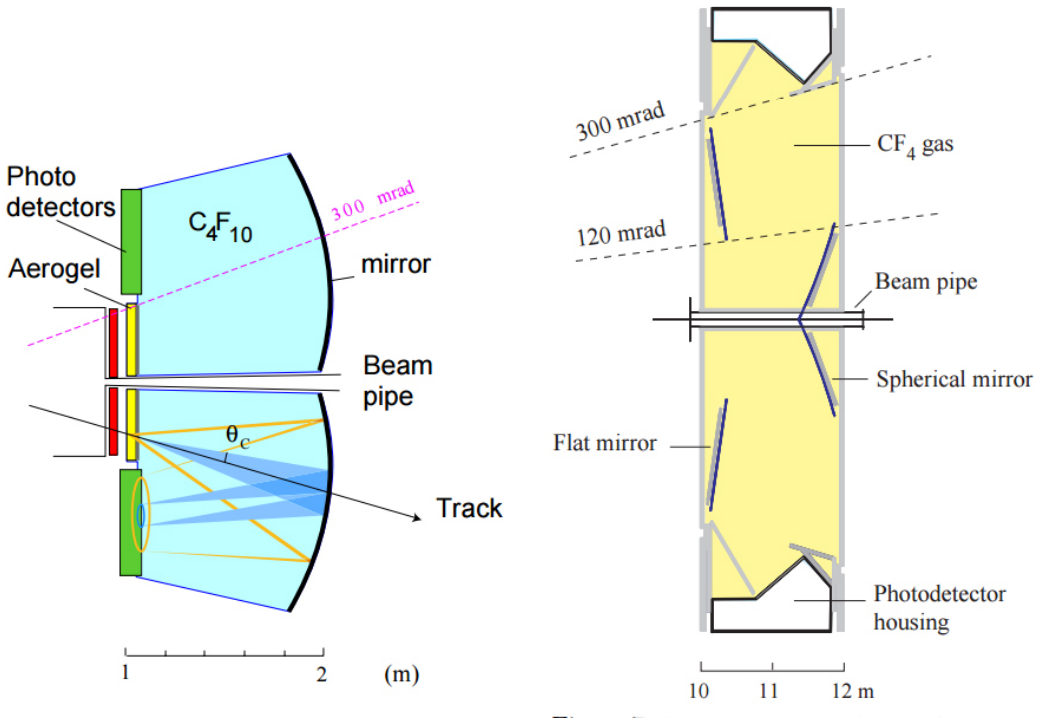

(a) (b)

Figure 2.1: Schematic layout of of the LHCb (a) RICH-1 and (b) RICH-2 detectors as seen from above[35].

The LHCb RICH-2 inner arrangement and mirror system can be seen on figure 2.1b. The mirror system comprises of two sets of mirrors, the primary spherical set and the secondary flat set. The spherical mirrors have a focal length of $f = 4000\,\text{mm}$ and are segmented into 56 hexagonal mirror segments inscribed into a circle that has 502 mm in diameter. They are arranged into two arrays, each with a common center of curvature having axes tilted by $\pm 450\,\text{mrad}$ horizontally with respect to the beam axis. One of this mirrors can be seen on figure 2.2.

The flat mirror array, on the other hand, is segmented into 40 square segmets of $437 \times 437\,\text{mm}^2$ each and the planes of these arrays are tilted by 140 mrad with respect to the horizontal.

Mirrors of both RICH-1 and RICH-2 are adjustable and their the mean mirror reflectivity over the wavelength range of interest is expected to be 0.9[35]. During the second long shutdown of the CERN accelerators in the year 2018, an upgrade is planned for the LHCb RICH-1 and RICH-2 replacing the Pixel HPDs with 64 Hamamatsu R11265 multi-anode phototubes(MAPMT) for the main regions of the detectors and 64 Hamamatsu H12700 for the outer regions of the LHCb RICH-2 detector[25].

As we will discuss below, the gain of MAPMTs significantly higher than the gain of the Pixel HPDs.

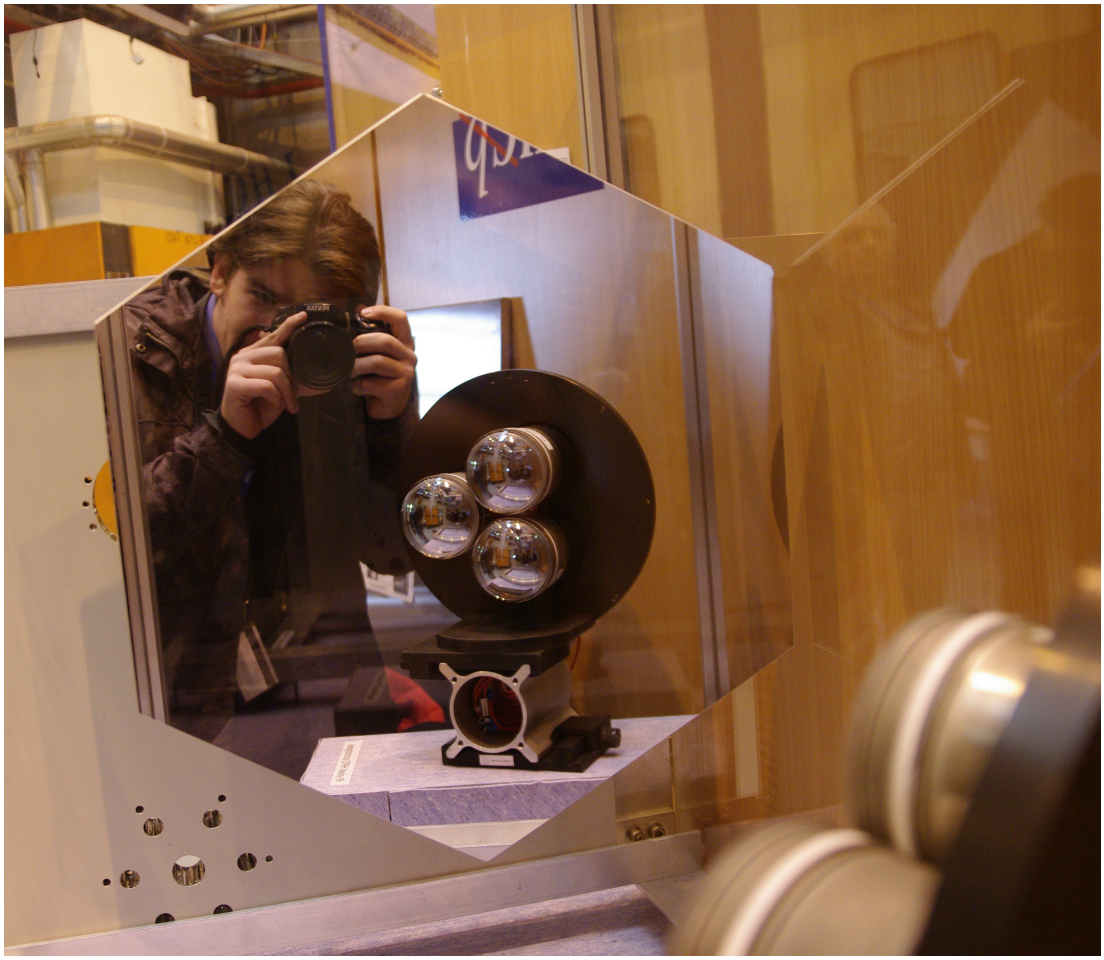

Figure 2.2: A mirror segment and a set of three hybrid photodiodes of LHCb. The COMPASS RICH-1 detector utilizes mirrors made from similar hexagonal mirror segments.

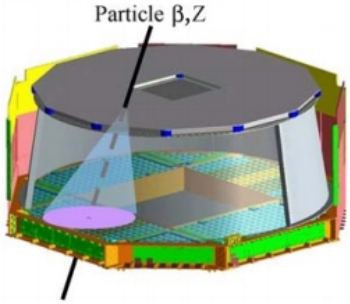

Figure 2.3: A schematic view of the AMS RICH detector[16].

2.2 AMS RICH

Another unique example of a RICH counter is installed at the AMS experiment. The Alpha Magnetic Spectrometer is installed on an International Space Station. It is a high energy physics spectrometer that's purpose is to detect cosmic-ray particles to shed light on mechanisms of cosmic ray production, acceleration and propagation important in the research of the dark matter.

For this task, AMS relies on RICH detector for an accurate velocity determination. The AMS RICH detector(as can be seen on figure 2.3) has a shape of a truncated cone with a top radius of 60 cm, a bottom radius of 67 cm and a total height of 60.5 cm. It contains a dual solid radiator made of 27 mm thick aerogel tiles in the outer region of the detector and 5 mm NaF tiles in the center region of the detector with a refractive index of 1.05, supported by a 1 mm thick layer of methacrylate(which has the same refractive index as the radiator) with an expansion height of 46.9 cm. This option of the radiator was chosen because of the restraints of the spaceflight, which limits the weight and the range of usable materials available for the construction of the detector.

These factors plus the need of a high magnetic field in the detector have driven to the choice of MAPMT as the photon detection system. The AMS contains a total of 680 16-anode PMT readout cells.

Figure 2.4: A model of ALICE experiment with the cherenkov counter visible in the top section as seven red blocks inside the red casing of the detector.

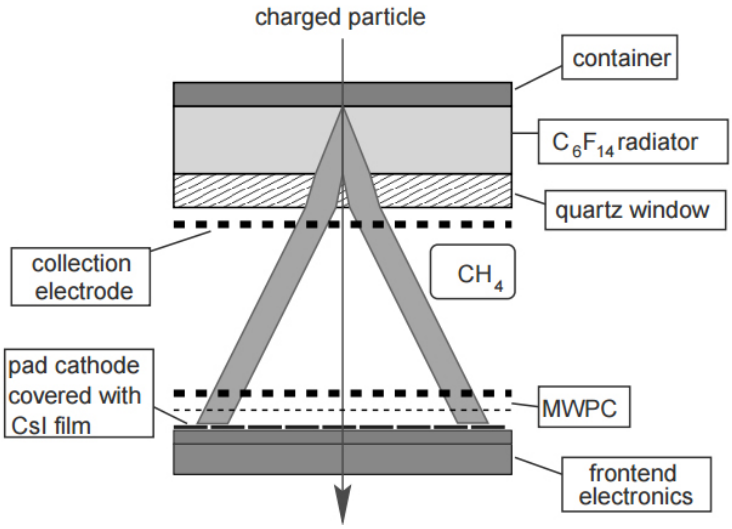

Figure 2.5: A schematic layout of the ALICE HMPID RICH module[7].

To minimize the amount of material in front of the electromagnetic calorimeter underneath the RICH, it contains a square-shaped hole in the middle of the detector.

The counter also utilizes a high reflectivity mirror to increase its acceptance.

Using this experimental setup, the AMS RICH is capable of reaching gains as high as $\sim 10^6$[16].

2.3 ALICE HMPID

A Large Ion Collider Experiment, is a general-purpose, heavy-ion detector at the CERN LHC. The model of this experiment is depicted on the figure 2.4. It was built mainly for research in the field of the quantum chromodynamics of the standard model. It consists of a central barrel part surrounding the collision point covering angles from 45° to 135° embeded in a large solenoid magnet and of the forward muon arm covering 2°-9°. The ring imaging Cherenkov detector or the high momentum PID detector(HMPID) is located in the central part of the experiment.

The ALICE HMPID is an example of yet another design of RICH counters, which is due to the construction of the ALICE experiment, mounted in an independent support cradle constructed in a shape of a spherical segment(see figure 2.4). It is dedicated to measurements of hadrons at momenta greater than a GeV/c and is designed to enable identification of charged hadrons beyond the momentum interval attainable through energy-loss and time-of-flight measurements. It was designed to cover an acceptance of 5% of the central barrel phase space and its geometry optimized to measure two-particle correlations, which require a high opening angle.

It is split into seven independent RICH modules of about 1.5x1.5 m^2 each. Each module contains a 15 mm thick liquid C_6F_{14} radiator and a multi-wire proportional chamber(MWPC) filled with a methane gas utilizing CsI photocatode panels segmented into pads for the detection atop of it.

The perflourohexane liquid used in ALICE HMPID has a refraction index of $n = 1.2989$ at the desired wavelength of $\lambda = 175\,\mathrm{nm}$.

Because of the liquid form of the radiator, it was needed to implement a circulation system that purifies the C_6F_{14}. After considering the fragility of the radiator trays and the inaccessibility of the detector during the run, a system based on a gravity flow was chosen. To remove contaminants, filters are inserted into the circulation system.

The MWPC detectors adopted for the photon detection contain total of $1.4\,\mathrm{m}^3$ of pure CH_4 equally split into each RICH module operated several mbar above the ambient pressure. To maintain a high purity of the gas, the flow rate of the gas supply is five MWPC volumes per day. When the machine is not operational, the MWPCs are being flushed with argon gas.

The ALICE HMPID is an example of an interesting use of RICH modules utilizing gaseous electron multipliers for photon detection. Using this experimental setup, the detector reaches a nominal gas gain of 4×10^4[7].

2.4 COMPASS RICH-1

The studied RICH-1 at COMPASS experiment is of a simmilar shape and type as the RICH counters for the LHCb experiment. It comprises of a $3\,\mathrm{m}$ C_4F_{10} gas radiator, a $21\,\mathrm{m}^2$ surface of spehrical UV focusing mirrors and utilizes a hybrid system of MWPCs and MAPMTs[9]. Because of this detector's importance for this thesis, only a short description of the detector construction is made in this section. For more detailed description, see the Chapter 4.

3. Gaseous detectors

The working principle of gaseous electron multipliers is rather simple. All gaseous electron multipliers contain a suitable ionizable gas or another suitable ionizable medium, a convertor, in which the primary electron-ion pairs are produced by an incident radiation which are then separated by an electric field between detector electrodes surrounding the ionizable medium and drift towards the electrodes under which usually lies the electron multiplication structure where the electric field strength reaches a significantly higher values in which the electrons experience an avalanche multiplication or the Townsend multiplication, as is the phenomenon sometimes referred to, named by the discoverer of the phenomenon, sir John Sealy Edward Townsend[5]. The mean number of the electrons produced by the avalanche is called the "gas gain"[34]. The primary electrons accelerated by the high electric field in the multiplication structure ionize the medium in the structure producing a secondary set of electrons, which can be accelerated again to produce more electrons and so on. Using this process, electron multipliers achieve exponential multiplication of electrons.

Under the primary electron multiplication structure usually lies the secondary electron transfer structure, the secondary drift region, which can deliver electrons to either another, secondary, electron multiplication structure or readout electrodes. By measuring the signals produced by the electrons in the readout electrodes, one can detect and obtain information about the incident radiation, mostly an information about the incident radiation position, but sometimes also its energy and time of arrival.

The most used types of gaseous detectors are microstrip gas counters, pixel and dot detectors, MICROMEGAS, GEMs and MWPCs[29]. In the next sections we will describe the principles of function of some of the listed detectors.

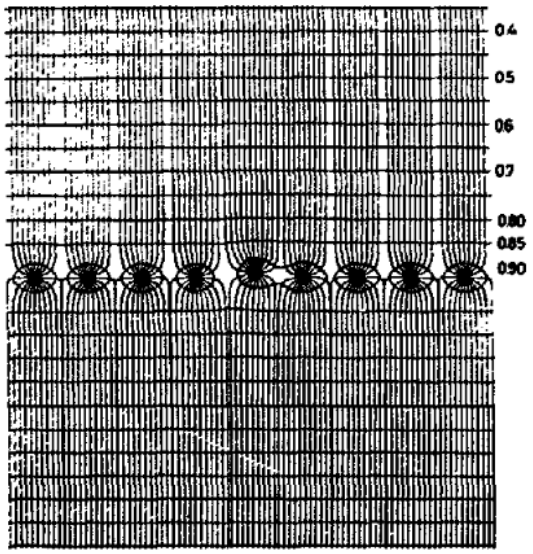

Figure 3.1: A visualisation of an electric field lines and equipotentials in the MWPC. An effect of a small displacement of one of the wires is also shown[28].

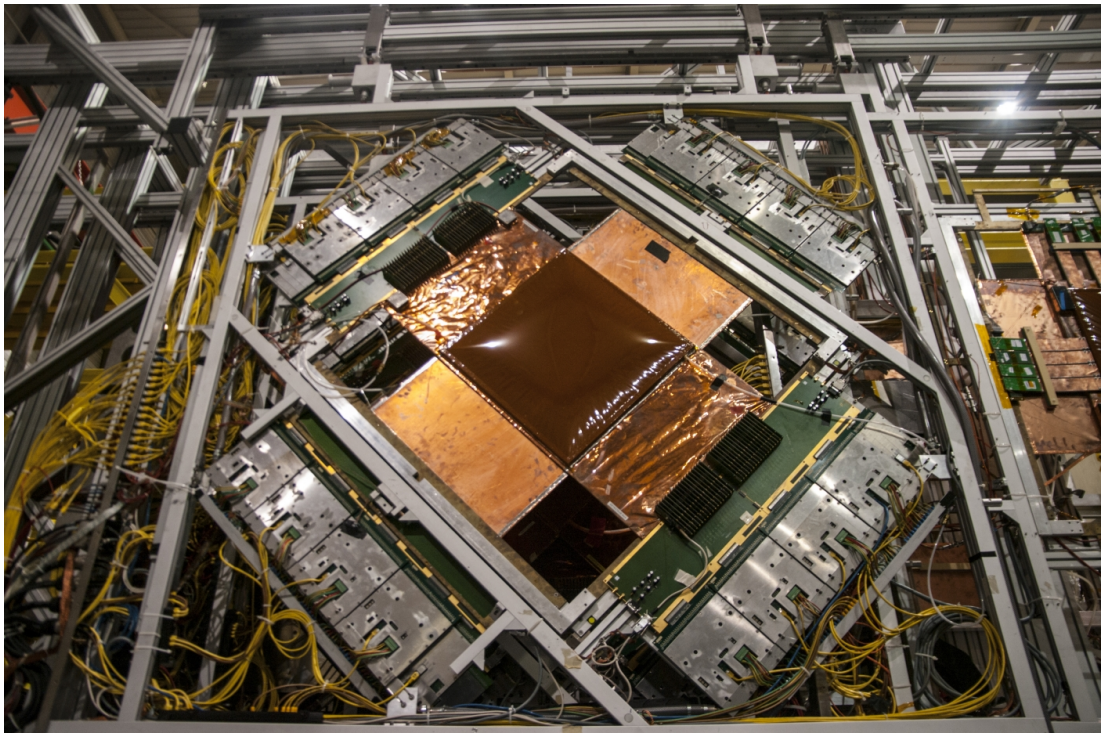

Figure 3.2: A MICROMEGAS detector on COMPASS experiment.

3.1 Multiwire Proportional Chambers and MICROMEGAS

Electron multiplication structure is the main difference between the listed detector types. The MWPCs are the simplest of the detectors listed. They consist of grounded cathode walls and a set of equally spaced anode wires. The electron multiplication avalanche effect happens in a region surrounding the anode wire. The size of the avalanche, comparable to the radius of the anode wire, is usually bigger than in the microstrip, microgap and microdot detectors in which the electron multiplication happens in a smaller region near the strips or dots. In all of these detectors(microstrip, microdot and microgap) the electron multiplication structure is discrete compared to a two dimensional structure of the MWPCs. A visualization of the electric field around the wires can be found on figure 3.1.

A modification of this design replacing the wires with a micromesh and placing the micromesh very close to the anode plane is the basis for the MICROMEGAS detector. In this case the micromesh is also a cathode, not an anode, contrary to the MWPC design. The advantage of the MICROMEGAS detector is its high position resolution due to a small gap between cathode and an anode and excellent rate characteristics[28, 29].

The first large-scale use of the MICROMEGAS technology was at COMPASS experiment[39]. The experiment still utilizes several MICROMEGAS detectors placed close to the target area, which can be seen on figure 3.2.

Figure 3.3: A sample of GEM plate placed under a microscope in CERN Microcosm exposition to show the scale of the holes etched in the Kapton foil.

3.2 Gaseous Electron Multipliers

GEMs are another different type of gaseous detectors. Unlike the MWPCs, they introduce a completely new electron multiplication structure consisting of two electrodes coated on a thin Kapton foil into which are etched small holes which, when a voltage is applied to the electrodes on the both sides of the foil, focus the electron inside them where the electron multiplication occurs. The process of creating the holes is well-described in [29]: "The detector is manufactured with photolitography technique. A metalized Kapton foil(typically roughly 60 µm) is coated on both sides with a photosensitive layer and exposed to UV light through a mask with the desired hole(typical diameter is 50-70 µm with a pitch or the distance between adjacent holes, of 140 µm) patterns. The metal is

chemically removed in the areas of holes and a second etching process extends these holes all the way through the Kapton." A sample of the resulting detector foil is shown on the figure 3.3. Advantages of the GEM detectors are its light weight, flexibility and high precision.

Holes in the GEM detectors are usually of a conical shape[22].

3.3 Thick Gaseous Electron Multipliers

As their name suggests, the difference between the GEMs and Thick GEMs, or ThGEMs for short, is the thickness of the region between the electrodes. To achieve the thickness and to simplify and reduce the cost of the production, the Kapton foil is replaced by a printed circuit board plate(usually 0.4-2 mm thick) and the holes reach typically bigger diameters reaching the same values as the thickness of the board itself and the detectors have a higher pitch, which allows for the holes to be drilled by a CNC machine instead of being developed via photolitographic methods and etched. This has advantage of significantly reducing the production difficulty and hence the cost of production. However, these simplifications take their toll as the spatial resolution of a such detector is significantly decreased compared to the spatial resolution of the classic GEM detector(about 5 times worse). However, such a resolution is sufficient for applications in RICH detectors and liquid noble gas time projection chambers[29].

Usually, a clearance ring free of coating is situated around the holes, called a rim, to avoid damages produced by electrical discharges[22].

4. COMPASS RICH-1

4.1 The COMPASS experiment

The experiment of NA-58 or COMPASS(Common Muon and Proton Apparatus for Structure and Spectroscopy) installed in 1999-2000 and commissioned in 2001 in the Prevessin site or North Area of CERN at the end of the M2 beamline of Super Proton Synchrotron(SPS)[36, 37] is a fixed-target experiment using a fixed targed, which can be polarized, to study a hadron structure and spectroscopy through the measurement of deep inelastic scattering and semi-inclusive deep inelastic scattering(2002-2011), the Drell-Yan(2014-2015) process and deep virtual Compton scattering(since 2016)[38].

The protons of the M2 beamline, which supplies protons with momenta of 450 GeV/c in form of separate spills lasting 8-10 s, leading towards the COMPASS experiment impact into a beryllium target T6 just before reaching the ground level producing desired hadron beam of particles with momenta 120-280 GeV/c, from which desired charge and momentum can be filtered using magnets with adjustable field strength and polarity placed some 700 m after the T6 target. To filter muons, which can be of 80-200 GeV/c, from the secondary beam, the beamline contains a hadron absorber.

The spectrometer itself consists of 3 parts, first of which contains beam monitoring apparatus before the polarized target, the Large Angle Spectrometer just after the polarized target, designed to have an angular acceptance of ±180 mrad and the Small Angle Spectrometer, designed to have an angular acceptance of ±30 mrad, each containing bending dipole magnets(SM1 and SM2 on Figure 4.2), trackers, muon filters, electromagnetic(ECAL1 and ECAL2) and hadron(HCAL1 and HCAL2) calorimeters. The Large Angle Spectrometer also contains the RICH-1 detector in addition to the already listed parts. The spectrometer itself is of a sandwich design and its length is roughly 60m.

It has underwent a major upgrade in 2005 during the long accelerator shutdown, gaining a new polarized target magnet and a RichWall slowly traversing

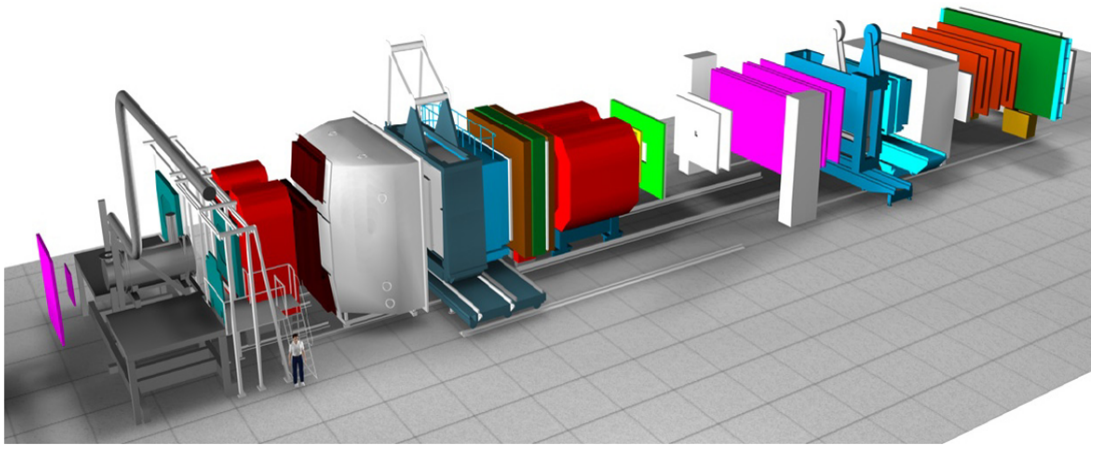

Figure 4.1: A visualisation of the COMPASS experiment in 2014[2].

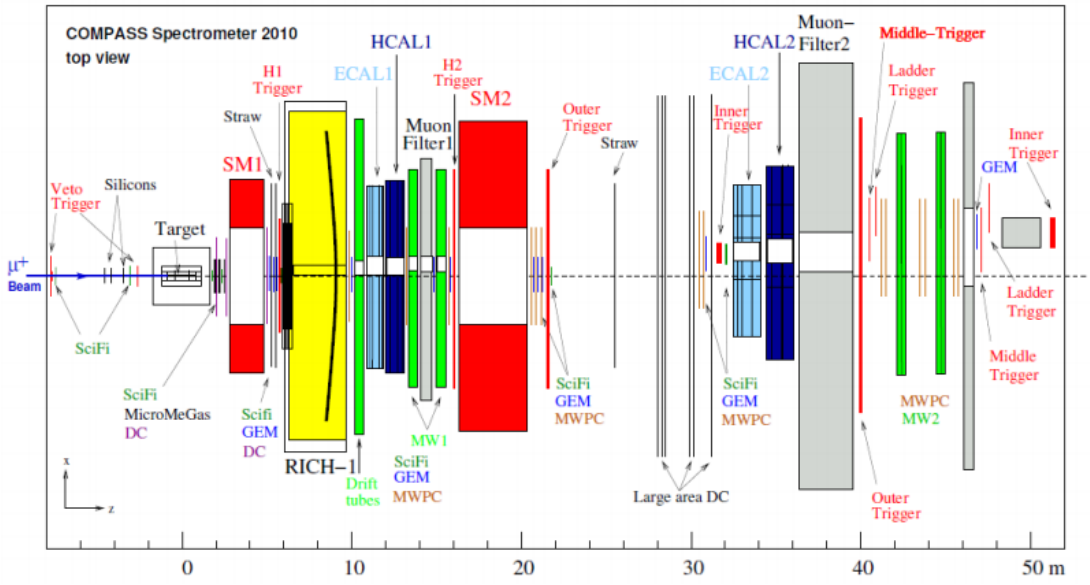

Figure 4.2: Setup of the COMPASS experiment in 2010[36].

into COMPASS phase II. The phase II started data taking in 2012[36, 37, 31].

4.2 Design and general features of the detector

The COMPASS RICH-1 is a large trapezoidal structure 6.6 m tall, 5.3 m wide and 3.3 m thick. The general layout can be seen on the figure 4.3. It has an angular acceptance of ±250 mrad in the horizontal plane and ±180 mrad in the vertical plane[13]. Its main purpose is to detect protons, pions and kaons. The thresholds of detection of each type of the particle can be read out of the figure 4.4, from which the lower detection thresholds for pions are roughly 3 GeV/c, 9 GeV/c for kaons and 17 GeV/c for protons, the upper threshold reaches as high as 55 GeV/c[13, 40].

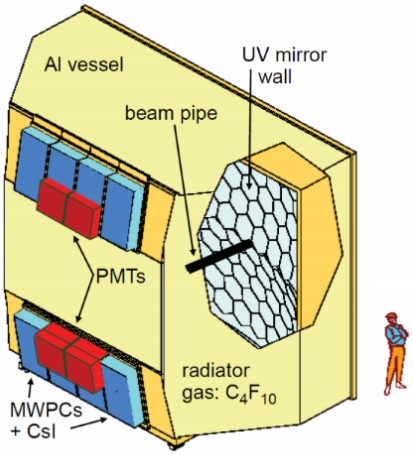

Figure 4.3: An artist view of COMPASS RICH-1[13]

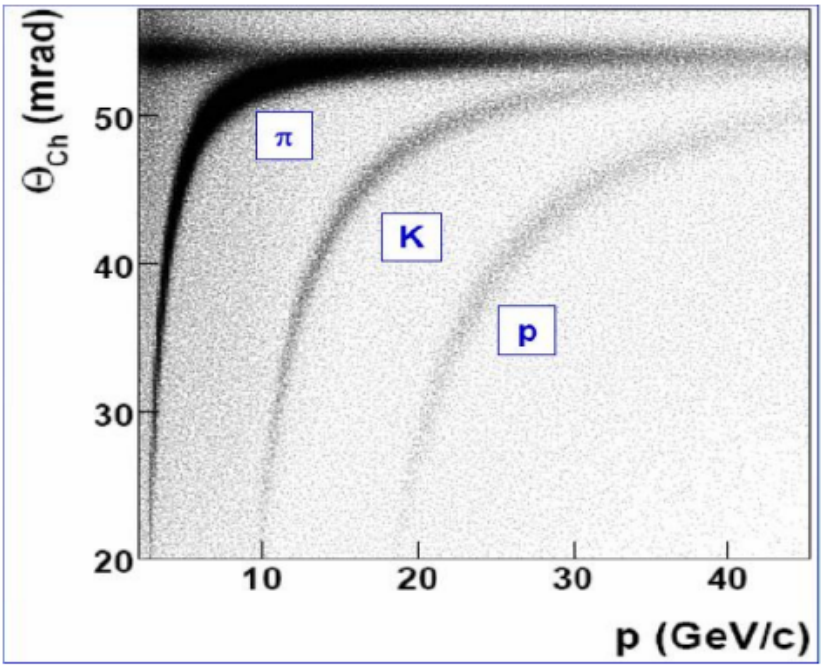

Figure 4.4: Distribution of the particle momentum versus the reconstructed ring Cherenkov angle. From this plot, lower momentum thresholds for various particles are visible[40].

4.2.1 The radiator

The detector radiator is a 3 m long gas vessel filled with $\sim 80\,\mathrm{m}^3$ of C_4F_{10} gas at atmospheric pressure and a constant, uniform temperature of roughly 25 °C. This setup provides transmittance higher than 80% for the desired $165 - 200$ nm photons. To ensure the purity of the radiator a decontamination system removing water vapour and oxygen traces has been implemented using molecular sieves. The system is sufficient to provide the decontamination from the UV absorbing impurities to the goal upper threshold of 5 ppm[17].

4.2.2 The mirror system and Continuous Line Alignment Monitoring

The focusing system of the COMPASS RICH-1 consists of two spherical mirrors. The mirrors are made from a 7 mm thick borosilicate glass on which 80 nm thick aluminium reflecting layer and 30 nm thick MgF_2 protective layer are deposited, and are a mosaic type composition of 116 spherical mirror units mounted on a net-like support structure with a clearance corresponding to 4% of total reflecting surface between them, of which are 68 of a regular hexagonal shape with 522 mm long diagonal and 48 of them are pentangonal units. The pentagonal units are used on the surface borders to avoid saw-teeth patterns. They are vertically displaced, up and down, by 1.6 m with respect to the beam axis. The arrangement results in a geometrical aberration of at least 0.32 mrad. The radius of curvature of the mirrors is $6600\,\mathrm{mm} \pm 1\%$, the diameter of the smallest circle containing 95% of the power associated with the image of a point-like source is less than 3.5 mm and the roughness of the mirror segments is less than 1.6 mm.

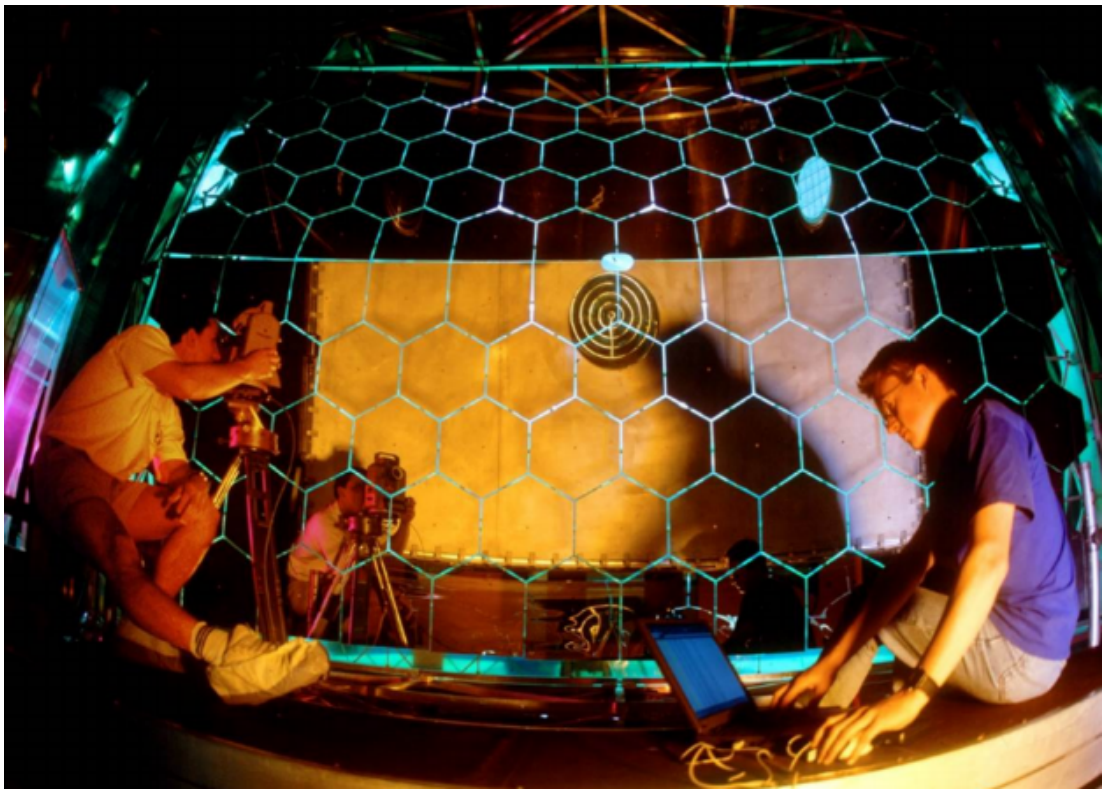

Figure 4.5: A photo of the mirror wall[44].

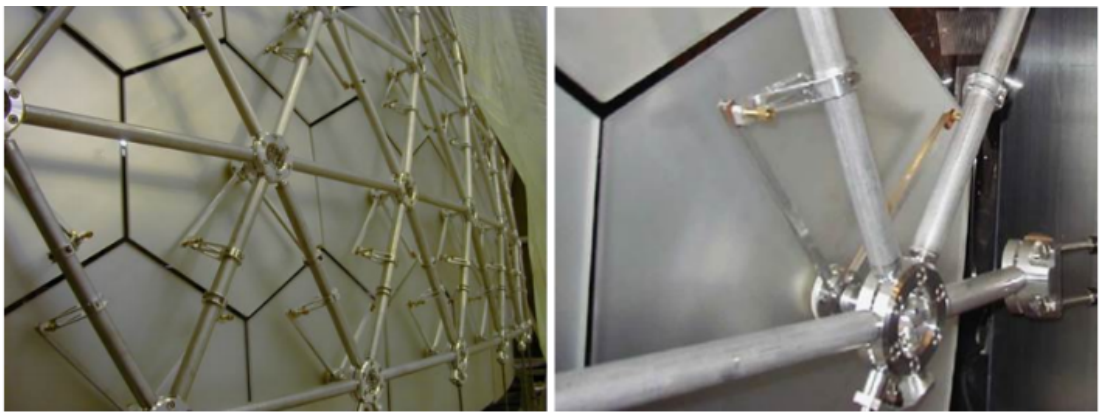

Figure 4.6: A photo of the support structure of the mirrors and of the adjustement screws[44].

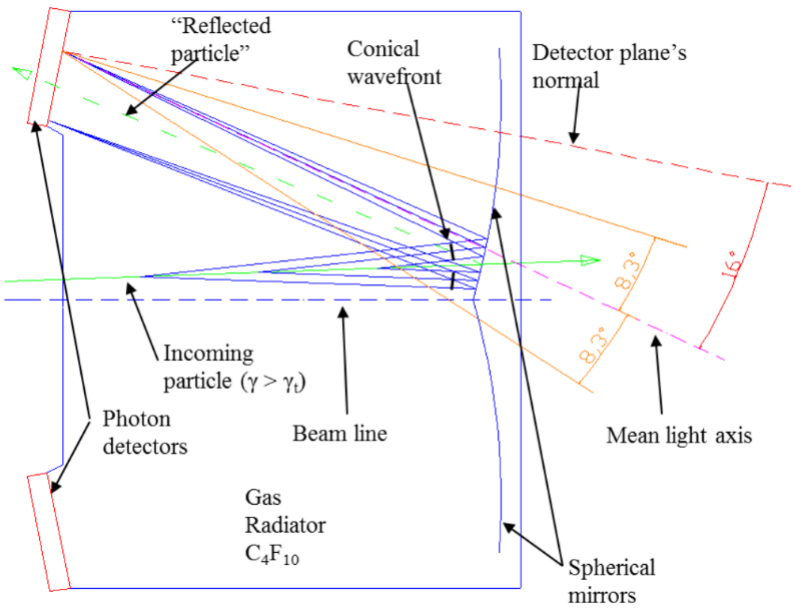

Figure 4.7: A schematic view of the COMPASS RICH-1 with the outline of a sample photon path[40].

Using this mirror composition, a reflectance of more than 80% is achieved for wavelengths above 160 nm. The mirror segmet mounts allow for a minor angular adjustments[18, 44]. The mirror wall can be seen on figure 4.5 and the mirror support structure on figure 4.6.

The alignment of the mirrors is a complex procedure involving flushing the radiator gas and working close to the mirrors, which bears a risk of damaging and contaminating the mirror surface reducing their reflectivity. In order to avoid this procedure and frequently monitor the mirror alignment during the data taking, an unique on-line mirror alignment monitoring method, called Continuous Line Alignment Monitoring method(CLAM), has been developed and implemented in 2007. It consists of four high resolution cameras fixed on the corner of the vessel and facing the mirror wall which record a reflected image of a rectangular retro-reflective grid placed close to the front wall inside the vessel illuminated by LEDs mounted close to the cameras[44].

4.2.3 The MWPC-based photon detectors

As the basis for the photon detection system at COMPASS RICH-1 detector serves a system of eight MWPCs divided into two groups of four detectors, one for the lower and one for the upper part of the RICH-1 detector[40]. Each of the MWPCs is equipped with two square CsI-coated photocatodes placed under a quartz window to convert the Cherenkov light into the primary electrons. The active area of a single MWPCs is $576 \times 1152\,\mathrm{mm}^2$ and each photocathode is segmented in pads. Each photocatode consists of 72×72, $8 \times 8\,\mathrm{mm}^2$ pads read individually by the readout electronics. This experimental setup gives us the total of 82944 channels. Each MWPC has its cathode wires with a diameter of 50 µm and pitch of 2 mm and anode wires with a diameter of 20 µm with the pitch of 4 mm and a anode-cathode gap of 2 mm. The MWPCs provide gain as high

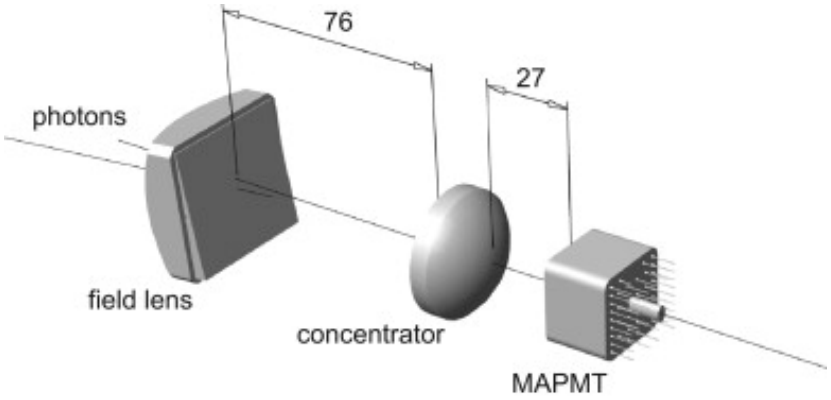

Figure 4.8: A schematic view of the MAPMT coupled with an optical two lens telescope. Measures are being given in milimeter[11].

as 5×10^4 which was the upper threshold beyond which the MWPCs rendered occasionally unstable.

In order to avoid the contamination by the air, especially the water vapour, which would have a deteriorating effects for the detector efficiency, a method of transport and storage in a controlled atmosphere with O_2 levels below 50 ppm has been developed[44].

4.2.4 The MAPMT-based photon detectors

With the start of a new, increased beam intensities and trigger rates and with the slow aging of the MWPCs, an upgrade was needed to cope with a longer detector dead time of 3.5 µs and to cope with the higher background near the beamline area, an upgrade for the COMPASS RICH-1 detection system was performed in the year of 2006[44]. Four of the MWPC cathodes in the center area, 25% of the total area of the detection system, were replaced by a fast photon detection system utilizing 576 16-channel Hamamatsu R7600-03-M16 MAPMTs each coupled to individual fused silica lens telescopes(scheme of which can be

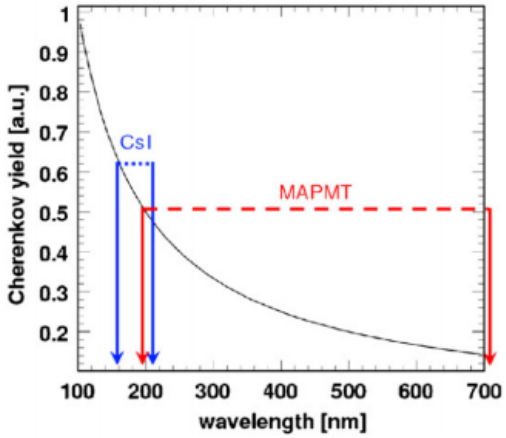

Figure 4.9: Cherenkov yield as a function of wavelength - comparison of sensitivities between CsI and MAPMT[8].

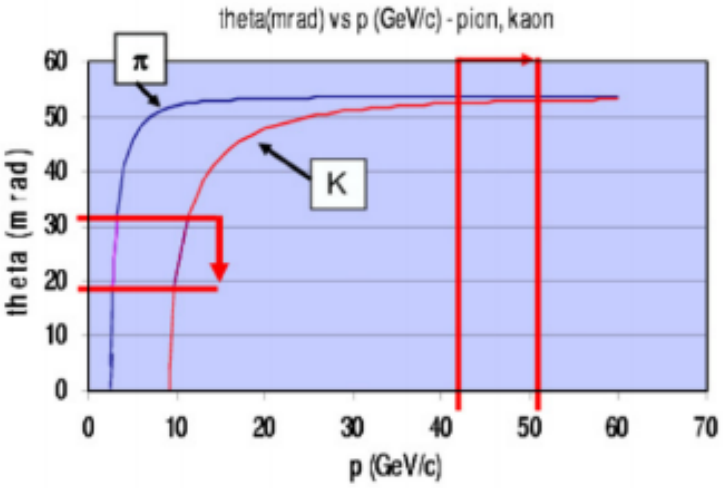

Figure 4.10: Simulated Cherenkov emission angle versus particle momenta - the PID capabilities extended by the detector upgrade are marked[8].

seen on figure 4.8)[10, 11]. As the result of this upgrade, the detector dead time was reduced to values between 400 ns and 3 µs and the data loss was reduced by nearly 5%[40]. The gain of the central area has been also improved, rainsing to levels of 10^7[13].

Apart from the improved readout characteristics, the MAPMTs have also the advantage of their bigger wavelegth range, increasing the detectable wavelength from 200 nm to 700 nm.. This drasticly improved wavelength detectability is best illustrated on the figure 4.9 and figure 4.10[10].

However, the use of MAPMTs brought a challenge. Because of the need for the large acceptance angle, an optical telescope system was needed to provide the focusing for the MAPMTs. A solution consisting of individual optical telescopes for each MAPMT unit was chosen to minimize the image distortion to avoid pixel cross-talk. The telescopes are 11.5 cm long and and have a full angular acceptance

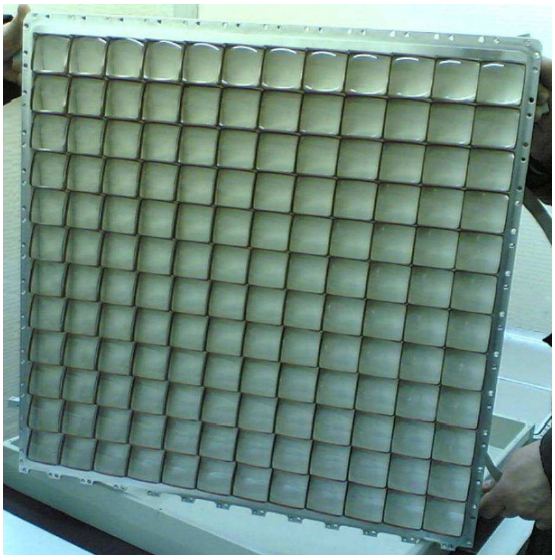

Figure 4.11: A frame hosting the field lenses[11].

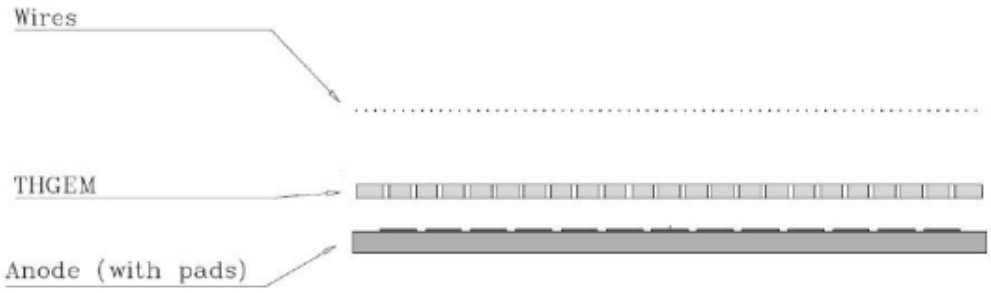

Figure 4.12

Figure 4.13: A scheme of a single ThGEM detector setup used in the characterization tests[24].

of 8.3°(which could be seen already schematically illustrated on figure 4.7) and a 50% acceptance as large as 9.3°. The telescopes are of a two-lens design: a field lens, which is plano-convex and have a 5° wedge, and a condenser, biconvex with one aspherical surface, lens, all of which have their surfaces coated with a MgF_2 antireflection layer. To support the telescopes, an elaborated mechanical design of frames was developed(can be seen on figure 4.11) allowing to reduce the dead areas of the detector below 2% of the surface[11].

4.3 Research and development of the ThGEM-based photon detectors

To replace the aging MWPCs and to meet the rising requirements for the detection system, a new upgrade is needed for COMPASS RICH-1. The upgrade is needed to be cost-effective and superior to the MWPCs already installed and as an optimal solution for the upgrade is seen to be the newly researched and developed technology of ThGEM detectors or ThGEM-MICROMEGAS hybrid photodetectors. For this purpose, over 50 different samples of small - $30 \times 30\,\mathrm{mm}^2$ ThGEM prototypes have been characterized using soft X-ray and UV light sources[21], and numerous large-scale($300 \times 300\,\mathrm{mm}^2$) detector prototypes with various electron multiplication cascade designs were built and tested in INFN Trieste as well as in CERN test runs of November 2012 and August 2014[23].

4.3.1 Small sample tests

The characterization of the 50 small-scale ThGEM prototypes was done with the prototypes filled with a gas mixture of argon-carbon dioxide in the ratio 70/30. The prototypes manufactured with a various parameters of rim size, thickness and hole diameters were irradiated using an intense X-ray source and the shorter and long-time gain evolution has been measured. The results of these tests are available to be seen on the figure 4.14.

The short-time evolution phenomenon(see figure 4.14a) explanation provided in the article of M. Alexeev [24] on which this section is based, is: "Due to the charge accumulation at the free dielectric surface present in the detector, the

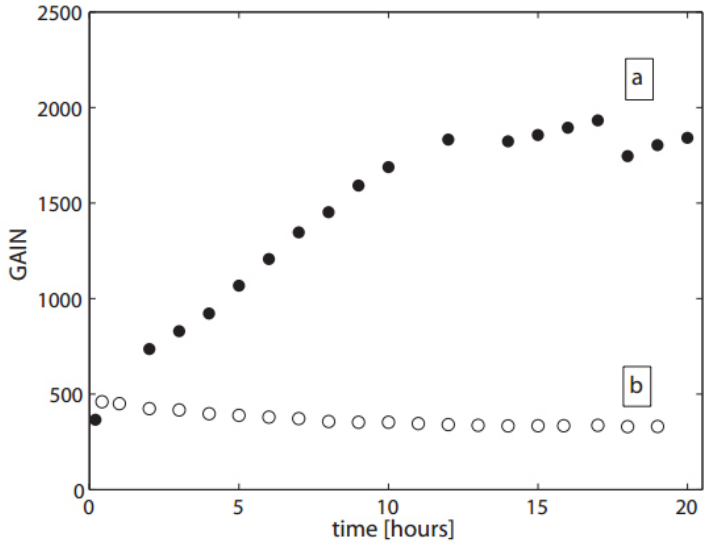

(a) Long-term time-evolution of the gain of two ThGEMs: both with pitch of 0.8 mm, hole diameter 0.4 mm and thickness 0.4 mm differing in **a** - rim size of 100 µm, $\Delta V = 1750$ V and **b** - rim size of 0 µm, $\Delta V = 1330$ V for continuous detector irradiation

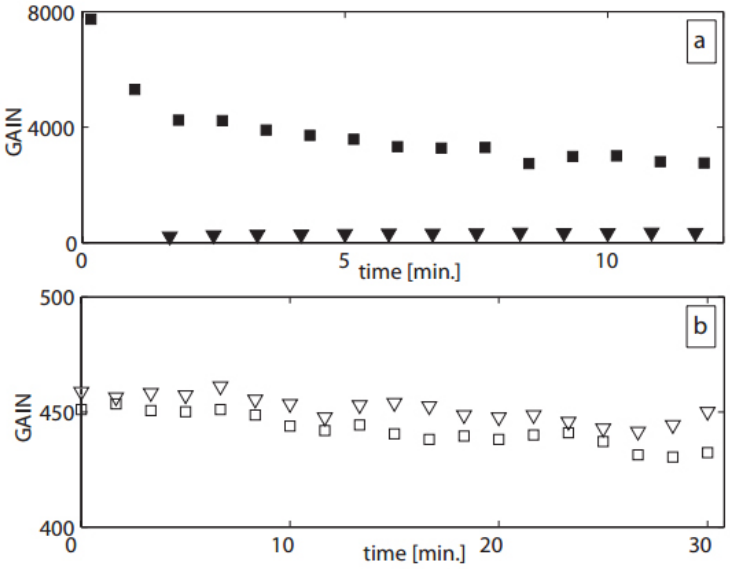

(b) Fast-time evolution of the gain of ThGEMs with pitch of 0.8 mm, hole diameter 0.4 mm and thickness 0.4 mm differing in **a** - rim size of 100 µm and **b** - rim size of 0 µm. Full(empty) squares: gain measured irradiating with an X-ray source the THGEM with large (no) rim after keeping it at nominal voltage for 10 h without irradiation. n. Full (empty) triangles: gain measured exposing to X-ray irradiation the THGEM with large (no) rim immediately at voltage switching on, after having kept the detector off for 24 h.

Figure 4.14: Long and short-time gain characterization of various ThGEM geometry designs[24].

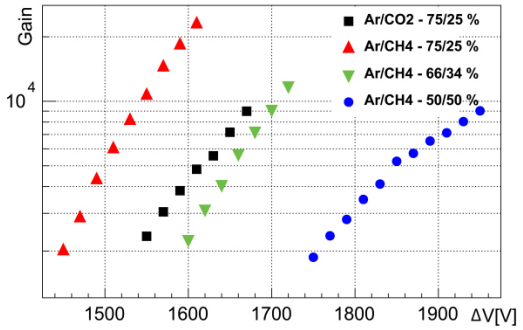

(a) ThGEM geometry: 0.8 mm pitch, 0.4 mm hole diameter, 20 µm rim diameter and the thickness of 0.4 mm

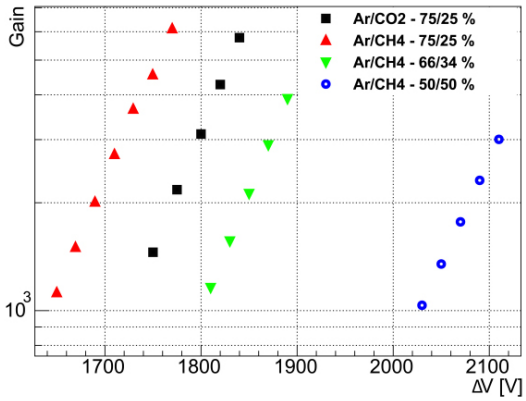

(b) ThGEM geometry: 0.8 mm pitch, 0.4 mm hole diameter, 0 µm rim diameter and the thickness of 0.6 mm

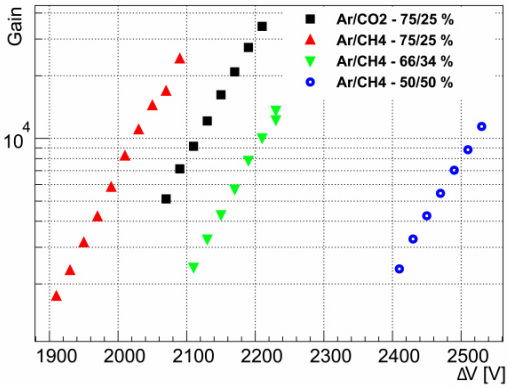

(c) ThGEM geometry: 0.8 mm pitch, 0.4 mm hole diameter, 0 µm rim diameter and the thickness of 0.8 mm

Figure 4.15: Gain achieved for different gas mixtures for a various ThGEM geometries[24].

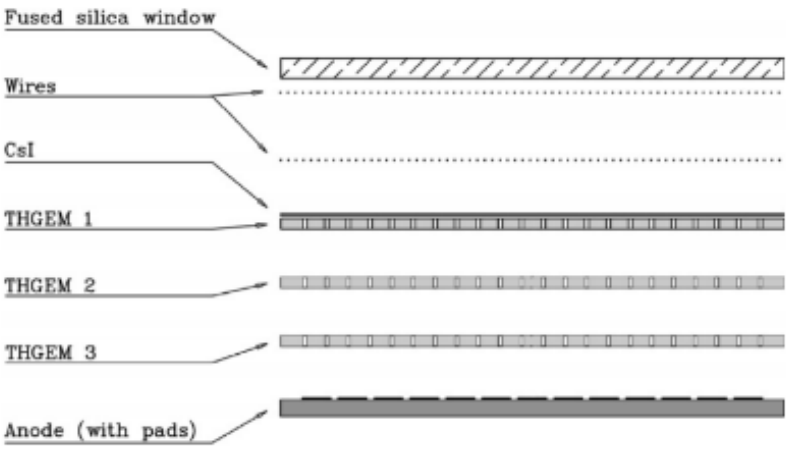

Figure 4.16: A scheme of a ThGEM based photon detector[21].

charge distribution and the time required to reach the asymptotic configuration depend on the amount of the open dielectric surface, the applied voltage and the irradiation rate, the charge accumulated at the free dielectric surface always reduces the electric field and this the detector gain and causing annoying detector discharges at switching on, when the rate at which the biasing voltage is applied is too high."

The long-time gain evolution on the figure 4.14b can be explained in terms of the charge mobility inside the dielectric, but regardless of the explanation, from the figure it is clearly visible the rim diameter advantage and disadvantage: ThGEMs with large rims, although exhibiting a much larger gains, provide a variable gain, while the ThGEMs with no rims provide almost constant gains.

A multiple ThGEMs were used to evaluate the gain dependency on the gas

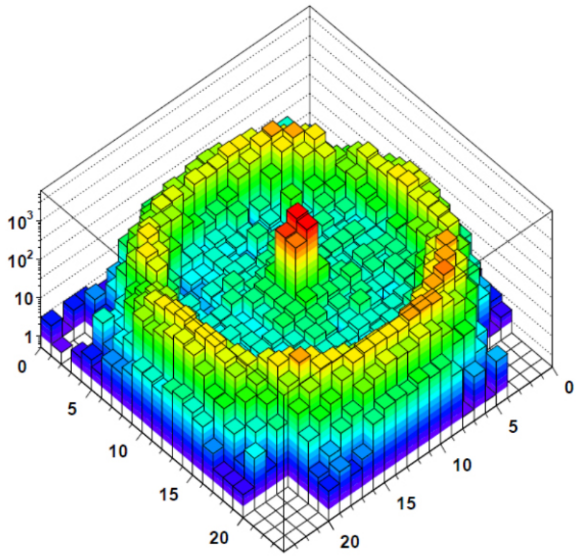

Figure 4.17: A logscale picture of the Cherenkov ring obtained using a 300 × 300 mm^2 ThGEM-based detector prototype during the CERN test run of November 2012[23].

mixture. The results are shown on figure 4.15. From studied geometries and gas compounds, a suitable geometry for the future runs has been chosen to utilize the most reasonable voltage difference of the ThGEM and maximize the gain.

4.3.2 The test run of Nobember 2012

The test run has been done in the East Area of the CERN Meyrin site in the T10 test area with π^+ beam of 6 GeV/c. It consisted of a chamber hosting two planes of wires and three ThGEMs all with a hole diameter of 0.4 mm, pitch of 0.8 mm, a rim of $\leq 5\,\mu$m and a thickness of the first, CsI coated ThGEM, 0.4 mm and the others of 0.8 mm. The detector scheme can be seen on the figure 4.16.

During this test, the detector was found to have the effective gain between 10^4 and 10^5, whilst the latter threshold was rather unstable. A picture of the cherenkov ring has been created using this detector setup, which can be seen on the figure 4.17[23].

During the test run, the triple ThGEM detector showed effective gains in the regions of the fifth order of magnitude, the thresholds being 0.9×10^5 for the lower bound with the voltage difference across the CsI-coated ThGEM of $\Delta V = 1350$ V with the time resolution of 11 ns and the maximum effective gain being 2×10^5 with $\Delta V = 1410$ V and the time resolution of 7.6 ns[20].

4.4 The CERN test run in August of 2014

The following section is based solely on the information acquired from the unpublished logbooks and personal discussions with the people of the INFN Trieste group during the test run of 2014.

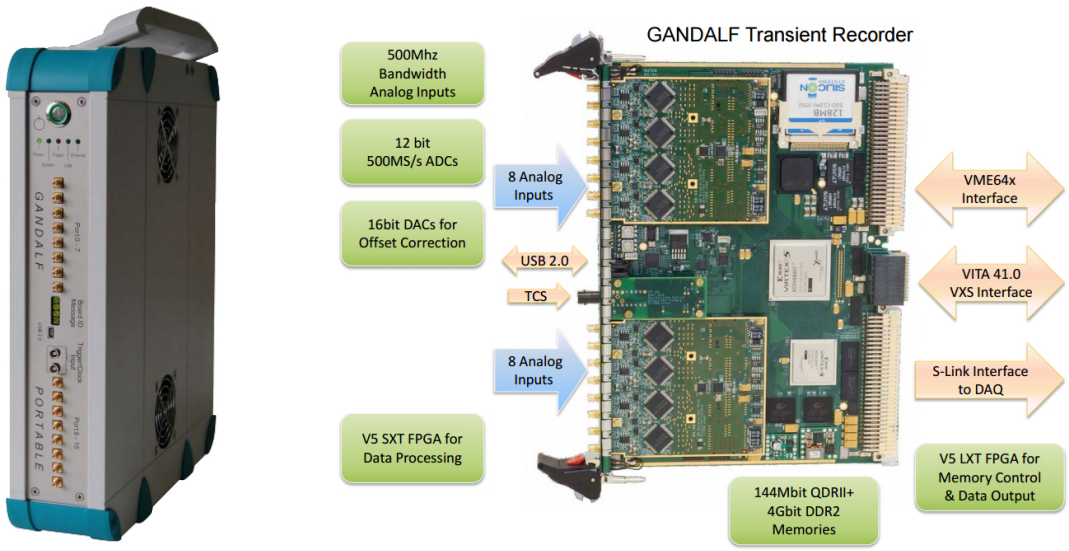

(a) (b)

Figure 4.18: The GANDALF analogue readout system. Figure (a) shows the portable unit used for readout of the single pad tests for the August of 2014 CERN test run, figure (b) shows the detail of a single GANDALF circuit board[41].

The test run of August 2014 at CERN consisted of three phases - first phase was testing of the prototype detectors in a laboratory at the CERN Prevéssin site, where the detector prototypes were tested fist partially assembled, without the CsI coated ThGEM, using a radioactive source employing ^{55}Fe isotope, in a chamber utilizing a kapton window.

The CsI coated ThGEM and a closing lid with a solid fused silica radiator(see figure 4.25) was then added to the chamber(the mounting has been done in N_2 atmosphere to avoid contaminating the CsI) and were then transported to the CERN Meyrin East Test Area and irradiated using a proton beam of the Proton Synchrotron T10 beam line with π^- particles with momenta of 5 GeV/c. First the performance of the detectors using minimum ionizing particles, MIPS for short, was evaluated. The testing was performed by directing the beam to one of the readout pads, amplified with Cremat CR-110 preamplifier and Ortec model 450 amplifier, which was then read out using analogue readout electronics system or analogue to digital converter(ADC) developed uniquely for the COMPASS experiment by the Freibourg group, Generic Advanced Numerical Device for Analog and Logic Functions or GANDALF(one of the GANDALF units and its PCB plate can be seen on figure 4.18)[41].

After the single-pad analogue measurement, a measurement using a set of digital readout electronics manufactured by the Torino group was performed on all pads.

The beam was then redirected to hit the radiator of the tested prototypes and the performance of the prototypes detecting photons was evaluated first by using the single-pad GANDALF readout, then by using the digital readout electronics.

4.4.1 Detector alignment and triggering mechanism

To align the detector properly, a rail system was utilized to ensure the horizontal alignment of the detector and two sets(one in front of the detector and one in the back of the detector) of two scintillators(so called fingers or crosses) equipped with step motors and one wide flat scintillator called pad(see the figure 4.19) were utilized to monitor the beam position using coincidence tuning(see figure 4.21).

The scintillators in combination with a multisampler clock(for synchronization) were also used as a trigger for the readout electronics. Although the CERN provided a start-stop signal when beam spills occured, the start-stop signal was present also in the absence of the beam inside the detector area(either by moving the beam blocker into position in order for it to be safe for personnel working inside the test area or sometimes in case of a beamline magnet malfunction). To ensure automatisation, a triggering mechanism based on scintillator detection was employed.

The overall triggering setup can be seen on figure 4.22, schematically on figure 4.20. The setup combined the signals of the both of the front scintillators and pad into a first, the front, AND gate, the back scintillators and the pad into the second, the back, AND gate and the signal of the front, the second AND gates, the pad signal and a clock signal(to control and synchronize the trigger) which was used for triggering the GANDALF system. As a veto served a tunable dual-timer allowing for veto windows in range of 1 to 100 µs of data taking. In this

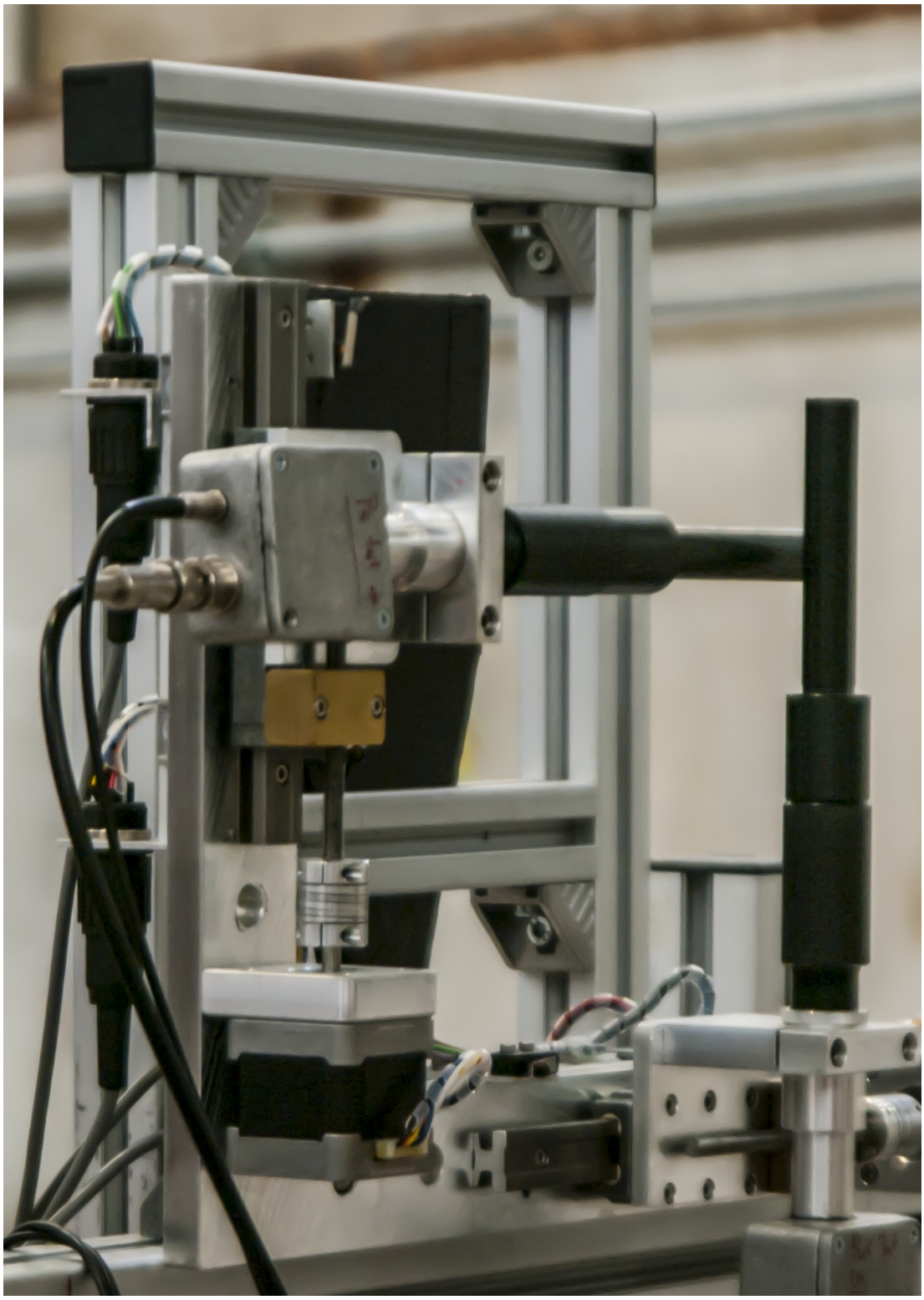

Figure 4.19: The scintillators used for the beam position finding and triggering.

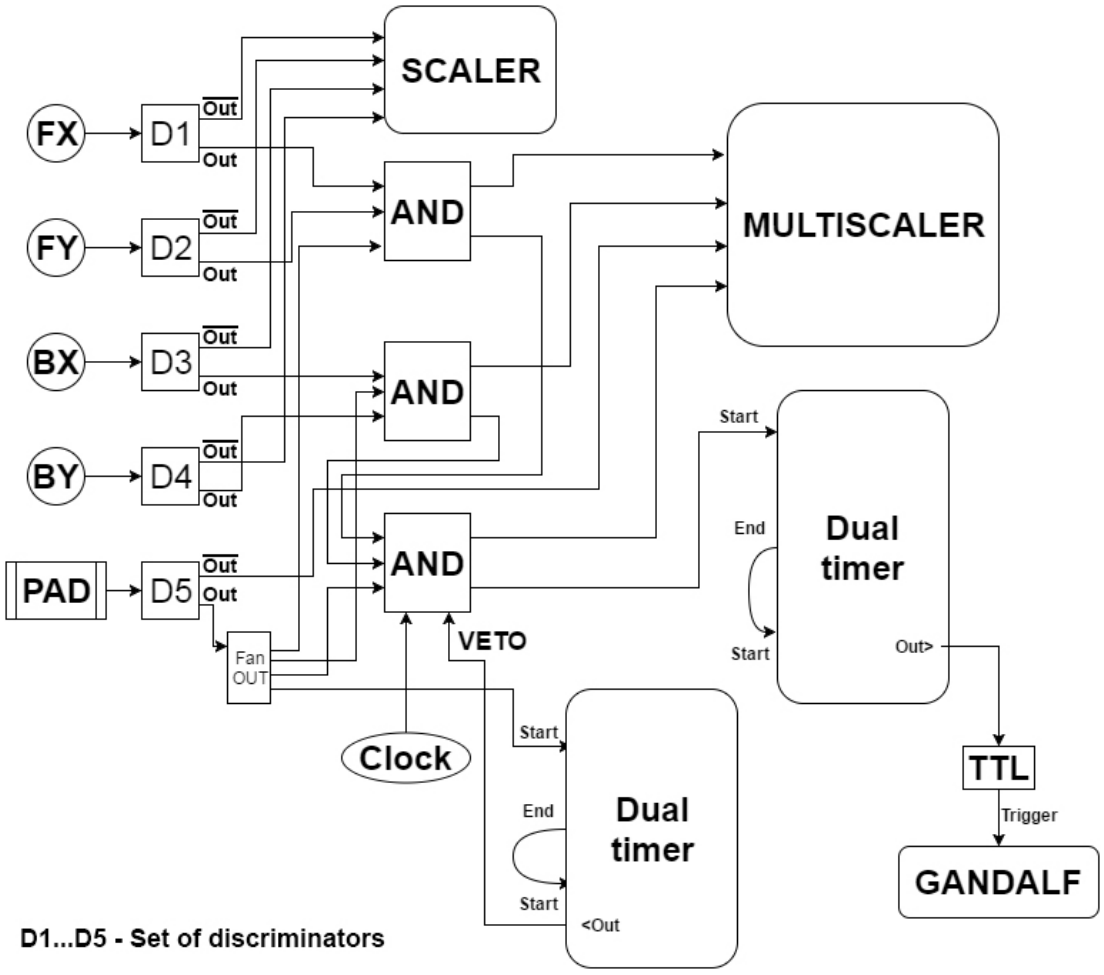

Figure 4.20: The trigger scheme of the trigger of the test run of August 2014. The TTL label just before GANDALF marks a NIM(Nuclear instrumentation module) to TTL(Transistor-transistor logic) translator.

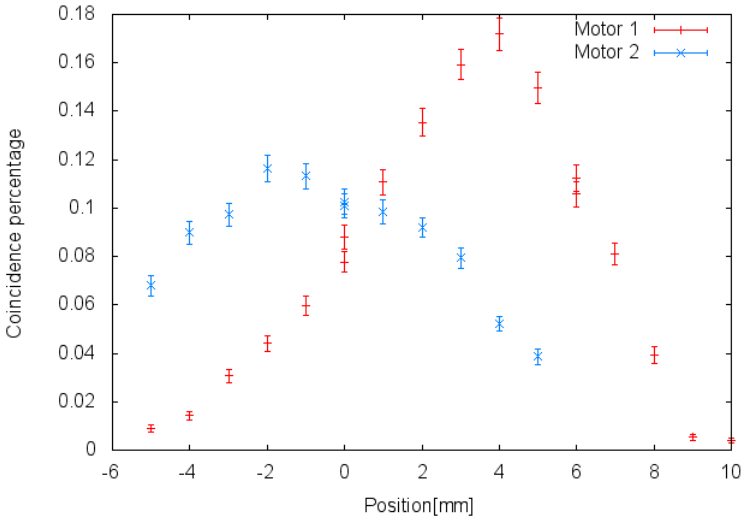

(a)

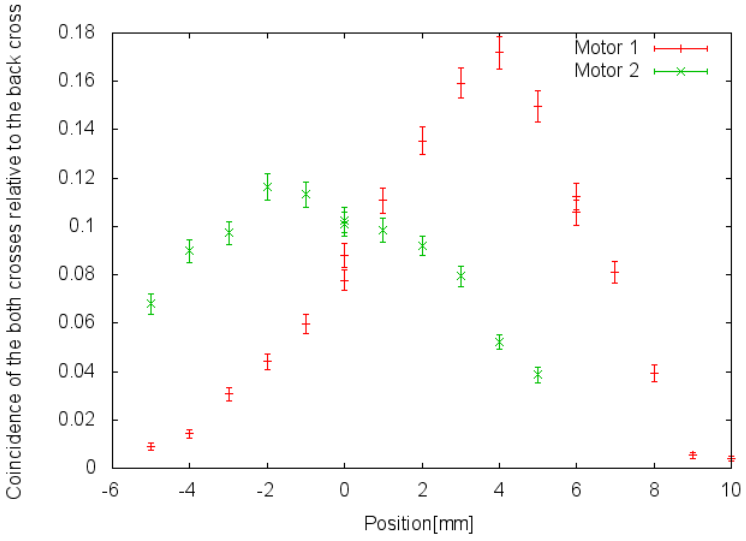

(b)

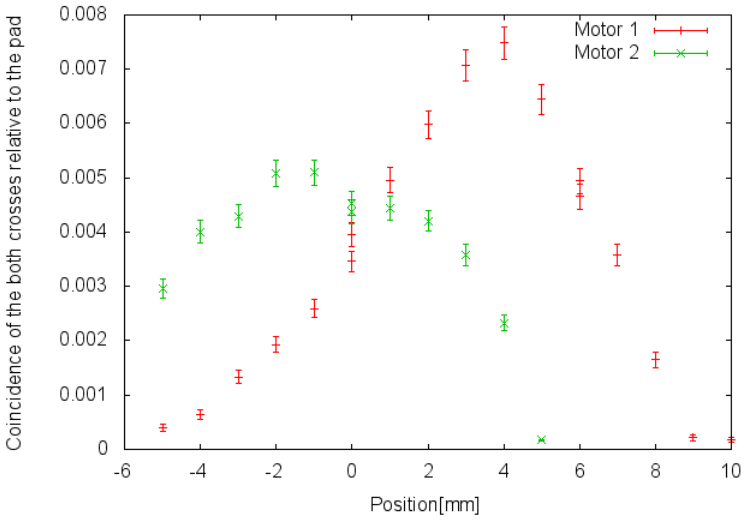

(c)

Figure 4.21: Coincidence tuning of the scintillators.

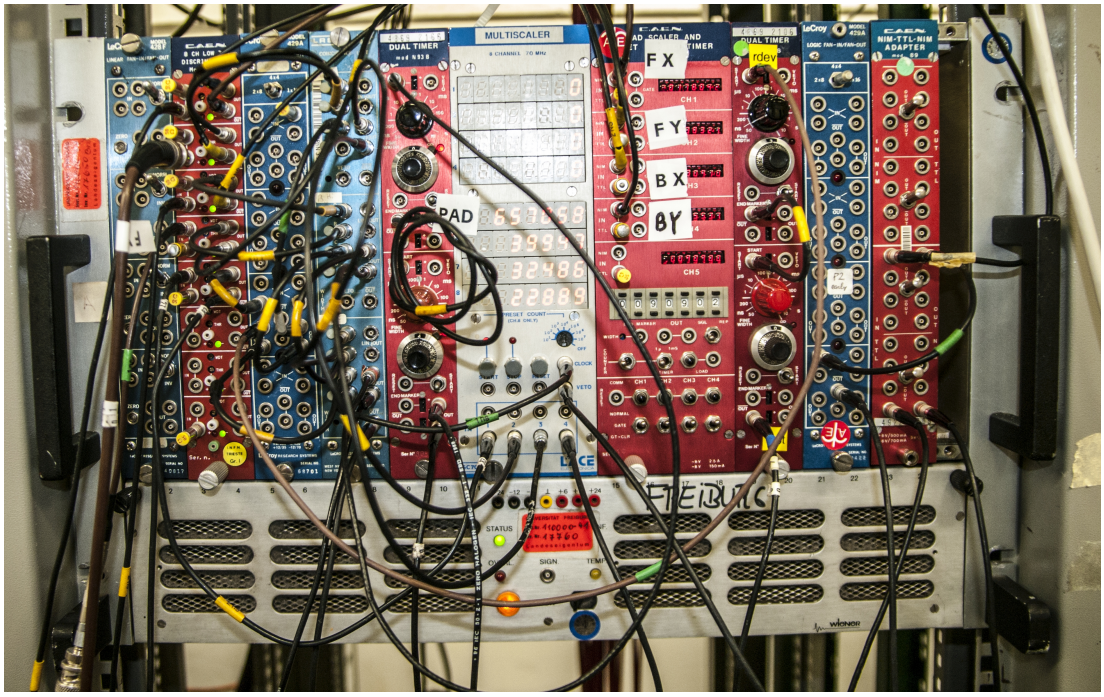

Figure 4.22: The setup of the trigger.

way, the triggering mechanism assured that there were no false triggers(triggers without traversing beam or triggers originating from the background radiation). For checking of incoming signals, one scaler and one multiscaler was used.

4.4.2 Detector prototype setup

Two detector chambers were tested, one called Big Sparky, the other Big Beauty. Both of the chambers were of a hybrid design and contained two ThGEM plates and one MICROMEGAS mesh. The scheme of them both can be seen on the figure 4.23. The difference between Big Sparky and Big Beauty was in their micromesh voltage, while the first had the micromesh(supplied by Scalay) placed under high voltage(HV) as standard, the latter had a resistive/capacitive anode design where micromesh was grounded.

The ThGEM plates were gold-coated and CsI-coated at CERN and were 0.4 mm thick with 0.4 mm diameter of holes and the pitch of 0.8 mm with no rim. The close-up to one of the ThGEM plates can be seen on figure 4.24. All of

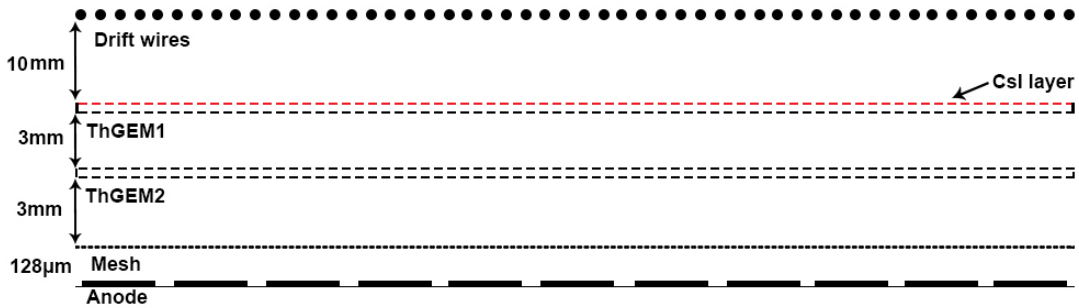

Figure 4.23: Scheme of the hybrid prototype detector chamber.

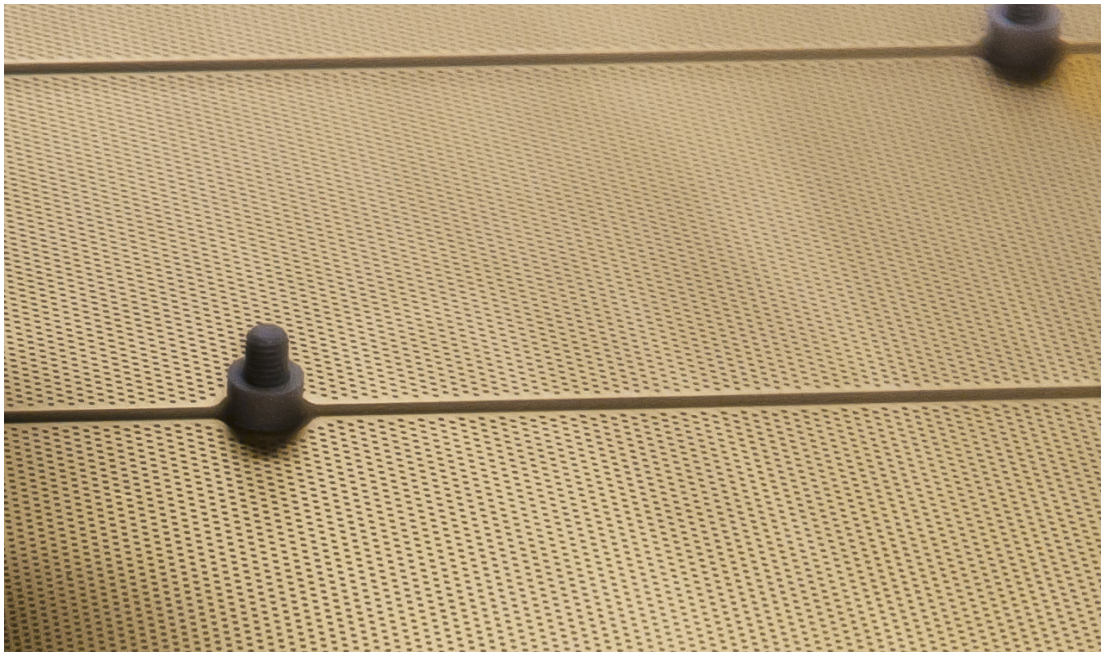

Figure 4.24: A close-up of the ThGEM plate installed to the detector chaber acting as a secondary electron multiplication structure. The detector holes and the support structure for the additional, primary, ThGEM detector plate can be seen.

the ThGEMs were segmented into 6 sectors for better voltage control, the top of each sector was connected to a separate voltage supply line, however, the bottom side of each plate was not separated as the top sides were. One of the plates and its division into sectors can be seen on figure 4.26.

Under the micromesh were 576, $11.5 \times 11.5\,\mathrm{mm}^2$ with 0.5 mm gap between pads, anodic pads or channels connected to a grid of $36(6 \times 6)$ readout pixels. A PCB with pads similar to the ones used in the test run of 2014 can be seen on figure 4.27. During all the operations done on the chambers(except for transport and mounting of the CsI ThGEM), the chambers were filled with a working mixture of 70% of methane and 30% of argon gas. A regular pressure and temperature checks have been done. The detectors worked in the East Area between temperatures of roughly 20 °C to 25 °C and pressures of roughly 962 mbar to 966 mbar. A sample day cycle of the temperature and pressure is shown on figure 4.28. The chambers were under constant gas flow of 20 liters per hour of methane and 8.6 liters per hour of argon.

At the Prévessin site, the gas mixture on the both detectors detector was 30% of carbon dioxide and 70% of argon flushed at the rate of 100 liters per hour, only lowered a day before the mounting of the CsI ThGEM plate to 10 liters per hour and after the mounting until its transport to the beam area it was maintained on 40 liters per hour.

For the testing of the detectors outside the beam area, a LED light was employed to provide testing photons.

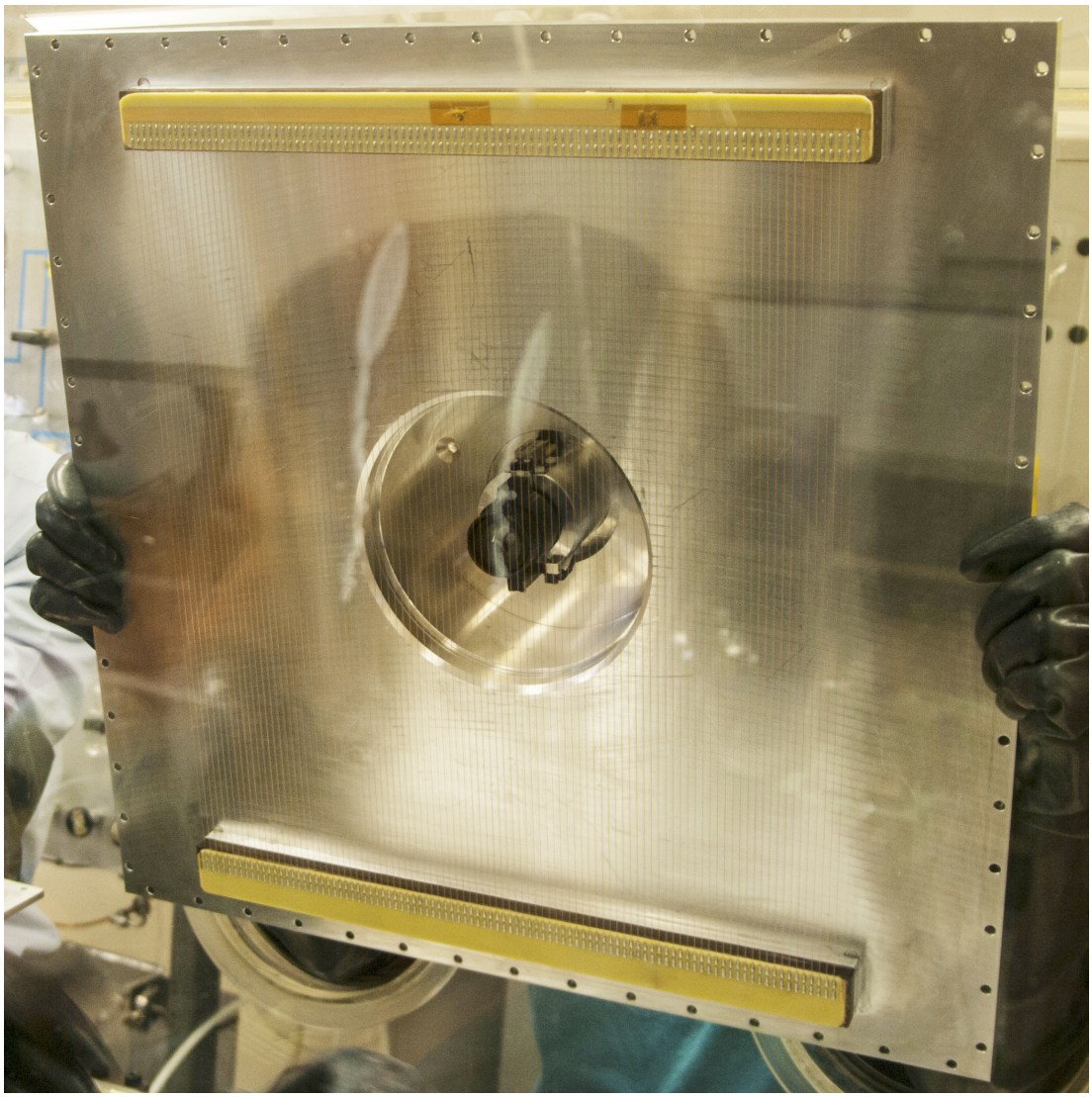

Figure 4.25: The close-up of the back side of the front wall or rather a "closing lid" of the detector chamber replacing a Kapton window after mounting the CsI coated ThGEM showing the fused silica solid radiator in the center.

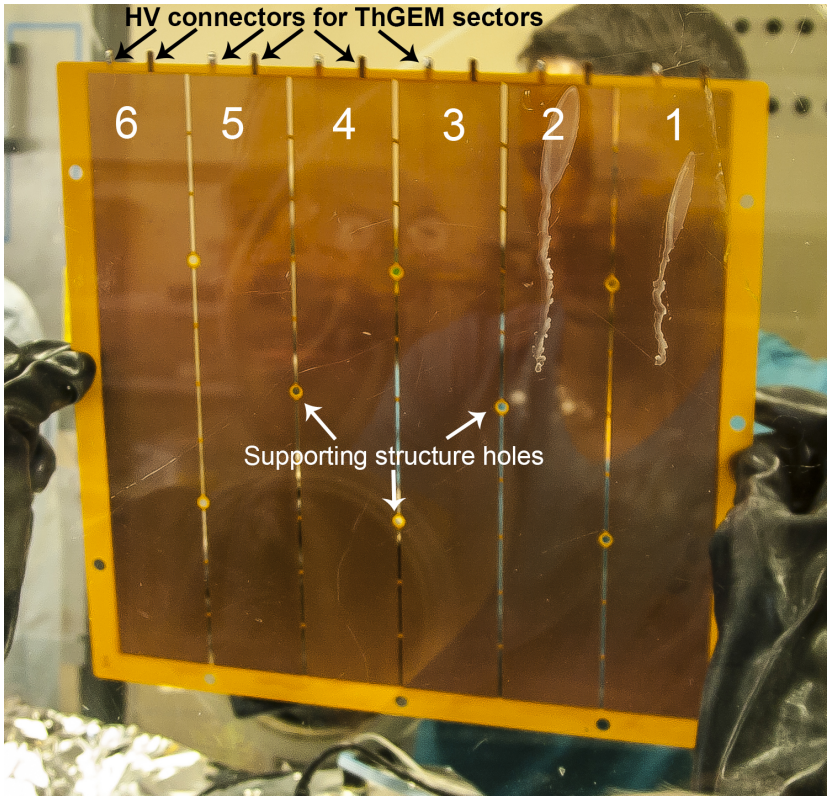

Figure 4.26: A ThGEM plate used in the August of 2014 CERN test run with the sectors numbering.

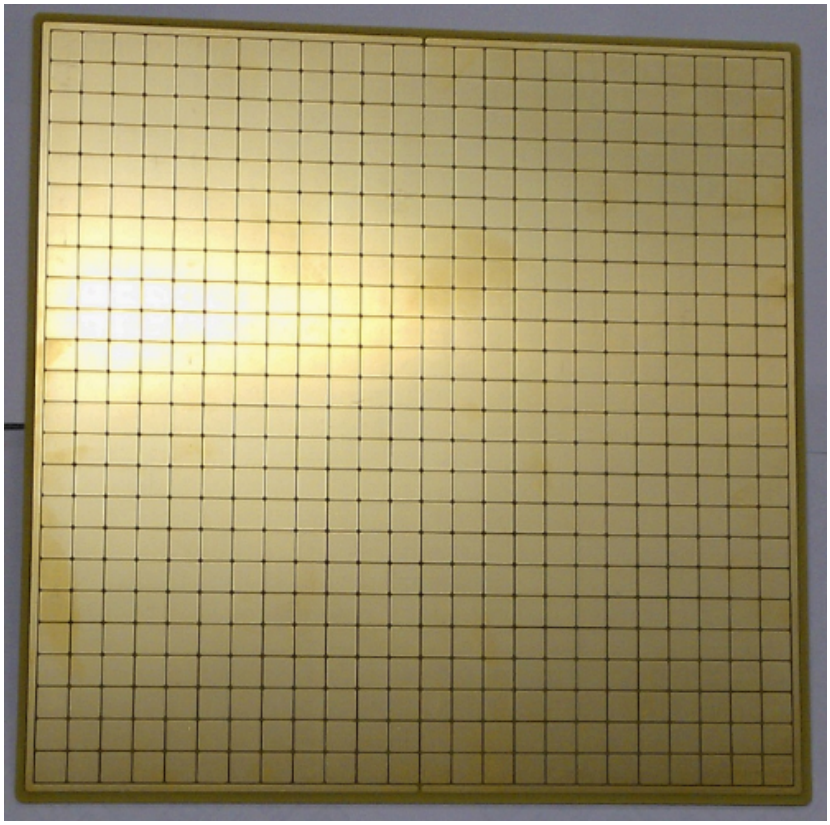

Figure 4.27: A $300 \times 300\,\mathrm{mm}^2$ PCB containing 576 pads[23].

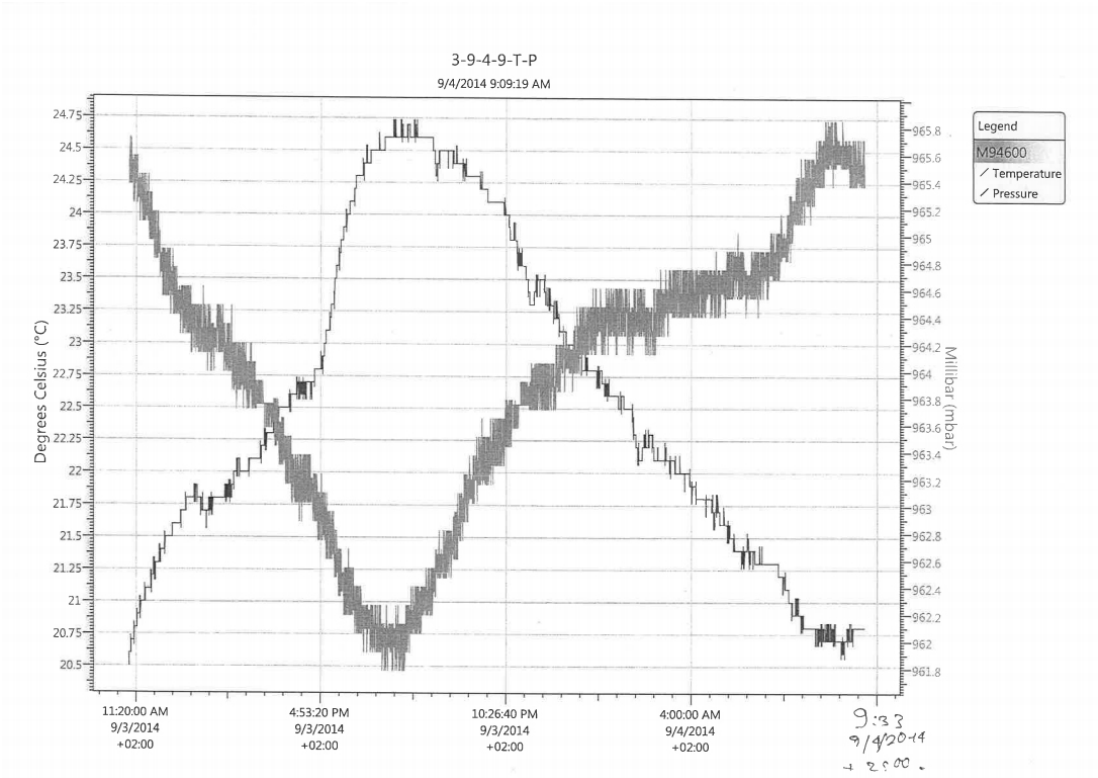

Figure 4.28: A sample day cycle of the gas temperature and pressure change.

4.4.3 GANDALF measurement

The most of the measurements done during the test run of August 2014 was done using the GANDALF device. The amplifier setup has been already described in the previous sections. Using this device, a spectra of MIPS and Cherenkov photons from a single pixel were obtained. Sample spectra histograms of photons can be seen on figure 4.29, sample spectra of MIPS can be seen on 4.31. Photon spectra can be seen to have exponential decay. This fact was explained in chapter 3. On the other hand, MIPS spectra are characterised by a landau distribution. It is this way because the electron avalanche created by MIPS is dependent on the energy loss of the MIPS in the medium of the detector, which is characterized by a landau distribution.

The collection of the MIPS spectra allows us to visualize the particle ionization collection dependency on the applied drift voltage, or drift scan. An average amplitude of the output pulse of the detector was calculated by fitting the landau distribution to the obtained histograms and calculating the area below the fitted landau curve. Sample spectra obtained using two different drift voltages can be seen on figure 4.31. These plots demonstrate the effect of the drift voltage on the pulse amplitude. We can see that with the increasing drift voltage, the anode detects more electrons of a wider energetic range, hence achieving a higher gain, while the lower drift voltage spectrum is much sharper and contain less entries.

From the collected data, a drift scan plot which can be seen on figure 4.33 was created.

The collected MIPS spectra also allowed us to compare micomegas gain dependency on applied voltage. The resulting outcome for the spectra can be seen

on figure 4.32. As we can see, even a small change in micromesh voltage can result in big differences in the obtained spectra. The overall dependency of the detector gain on the micromesh voltage can be seen on figure 4.36.

The gain of the MIPS spectra can be easily read out from figures 4.34 and 4.36, which can be seen exceeding the threshold of 10^4. The highest gain for the photon spectra was measured to be 1.3×10^4.

The same was done for the photon spectra of the Big Beauty detector, which achieved a higher gain during the test run. Obtained data were fitted using exponential function and the integral of the exponential fit has been extracted. This chamber has been performing well enough to enable the drift scan with two different noise thresholds. The resulting drift scan for photon spectra can be seen on figure 4.30.

From the collected data, a time resolution(how accurately the time at which a particle crossed the detector[4]) can be determined as the full width at half maximum of the incoming signal from the detector, as the GANDALF system provided a time stamp in its output. The time resolution of the hybrid ThGEM design has been found to be 9 ns. The pulse evolution with the highlighted time resolution can be seen on figure 4.35.

Obtained plots and dependencies will be vital in the final optimization of the performance of the final photon detector system for the COMPASS RICH1

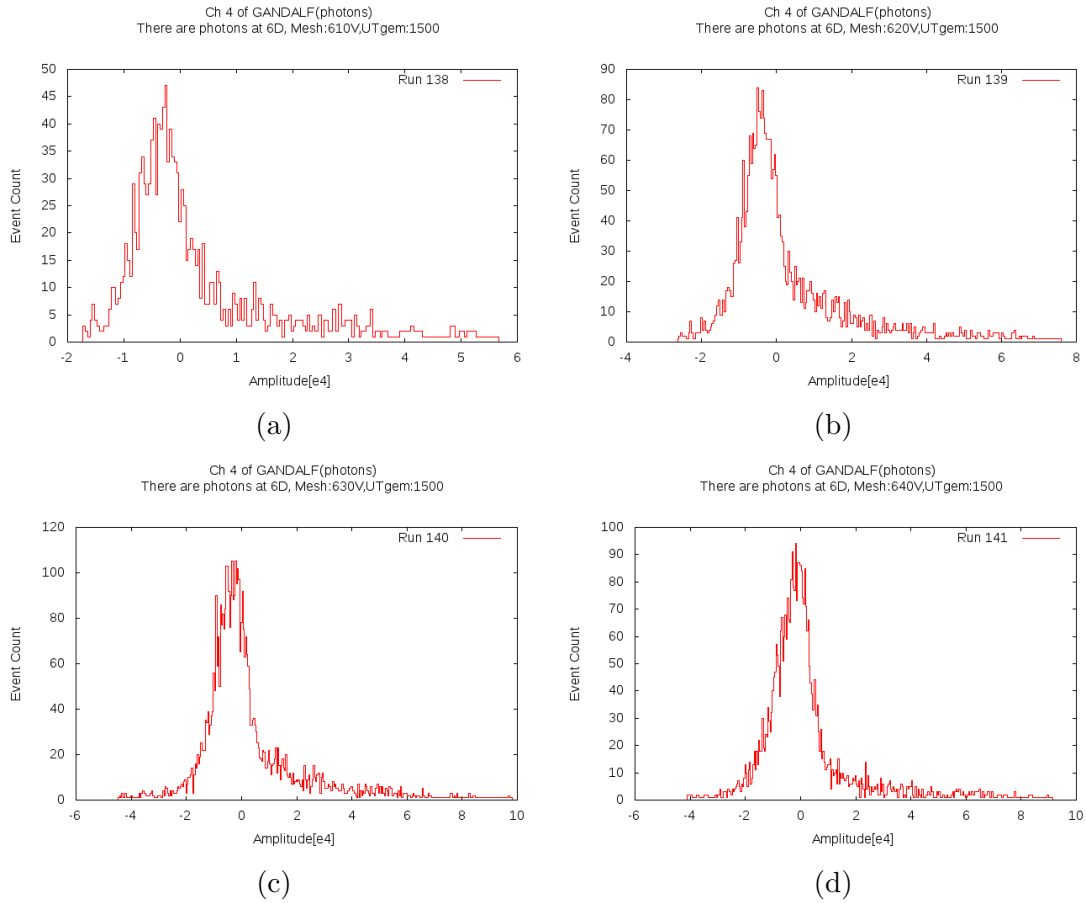

Figure 4.29: A sample set of photon spectra. Histograms made from raw data extracted from GANDALF. The x-axis is in tens of thousands of arbitrary units.

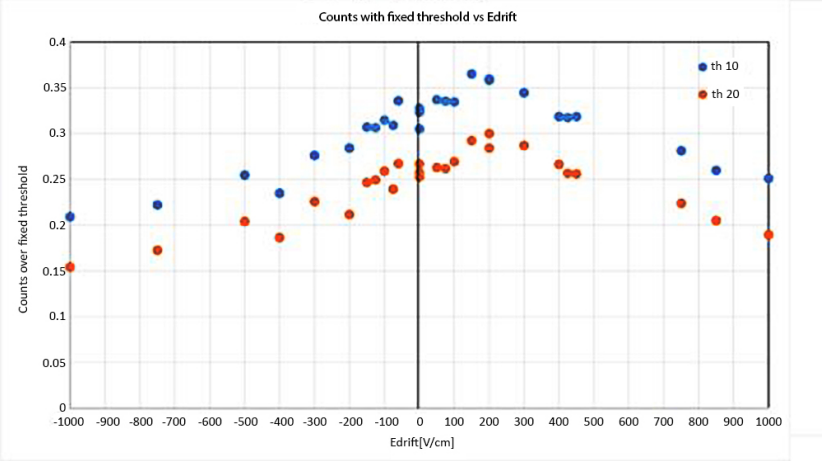

Figure 4.30: A drift scan from the Big Beauty detector for photons using two different noise thresholds[45]. Plot made by INFN Trieste group.

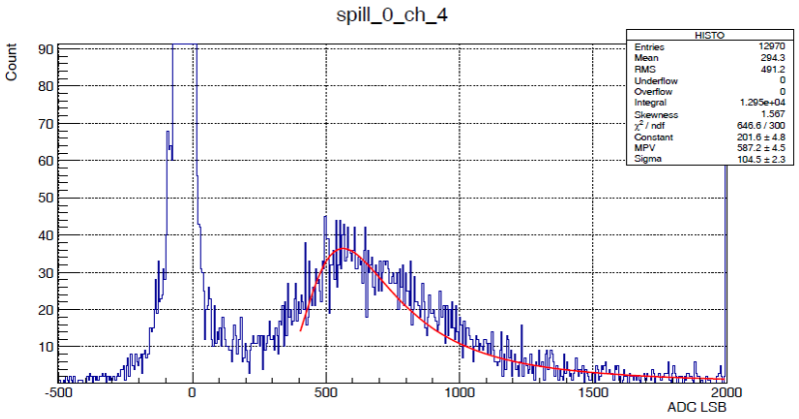

(a) $U_{\text{drift}} = 1000\,\text{V}\,\text{cm}^{-1}$

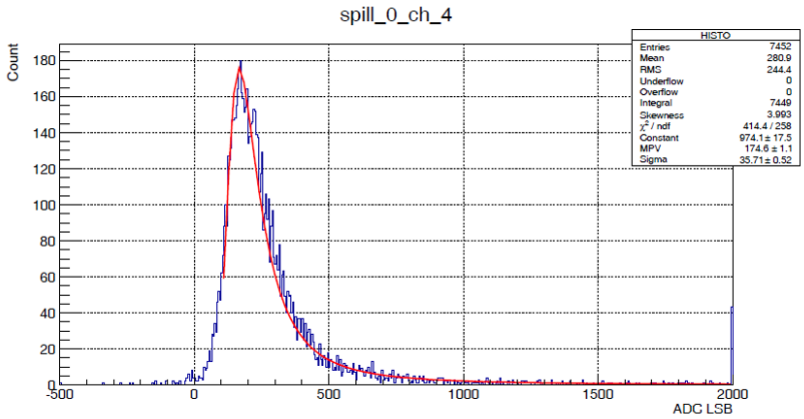

(b) $U_{\text{drift}} = -100\,\text{V}\,\text{cm}^{-1}$

Figure 4.31: Particle ionization collection dependency on the drift field shown on MIPS spectra[45]. A pedestal put in place by the GANDALF system to mark the zero-point of the histogram is visible on the figure (a). LSB means Least Significant Bit. Plot made by INFN Trieste group.

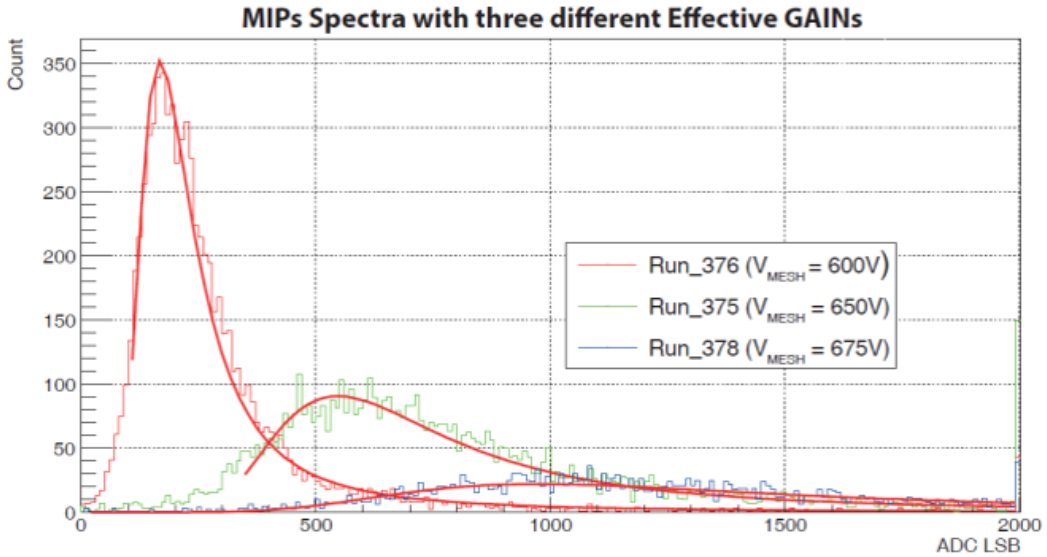

Figure 4.32: Micromegas gain dependency on applied voltage. The chart shows the MIPS spectra taken with different micromesh voltages[45]. Plot made by INFN Trieste group.

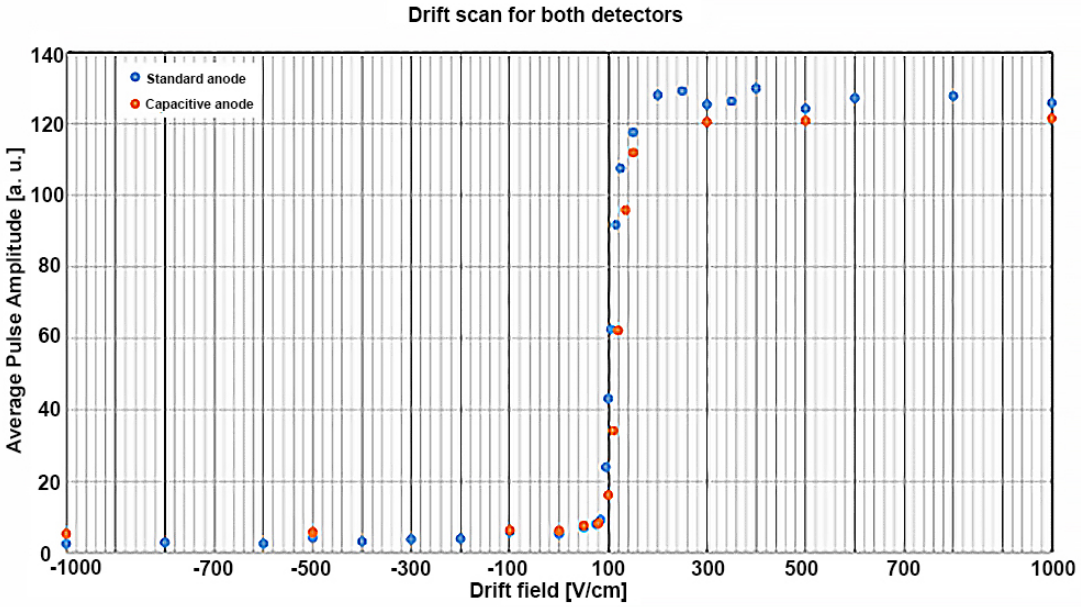

Figure 4.33: Charged particle ionization collection dependency on the drift field[45]. Plot made by INFN Trieste group.

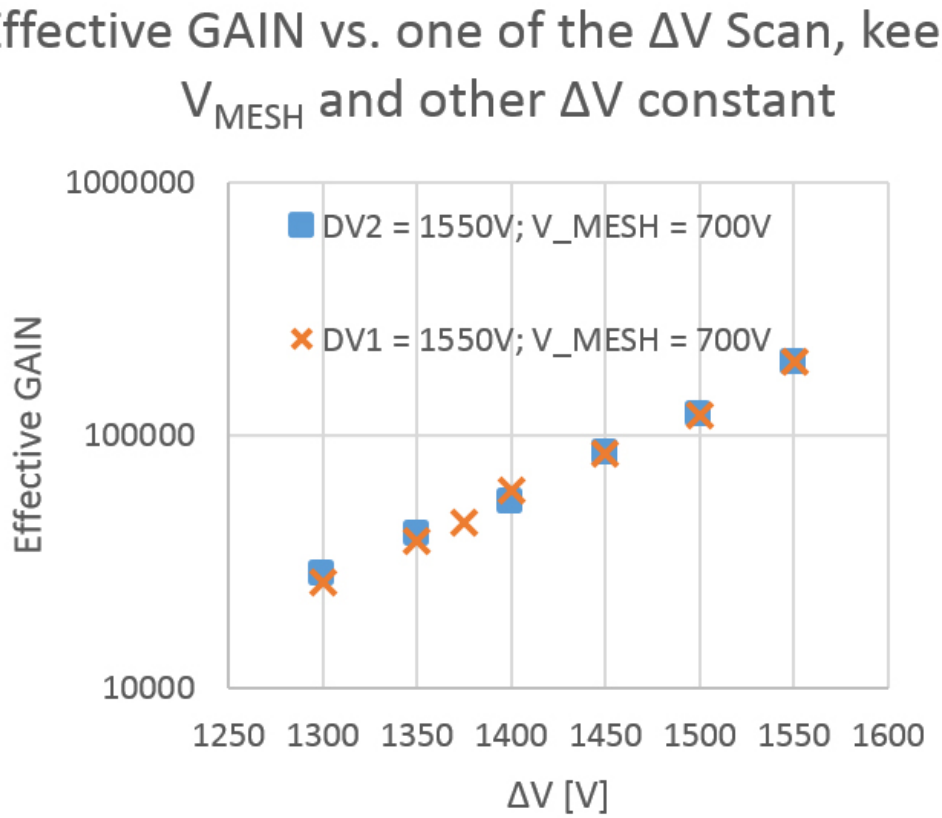

Figure 4.34: Dependency of the detector gain on the differences between the voltages between the top and the bottom side of the ThGEM1 while keeping the ThGEM2 ΔV(DV2) constant and ThGEM2 ΔV changing while keeping the ThGEM1 ΔV(DV1) constant. The micromesh voltage has been kept constant at the level of 700 V while acquiring this plot[45]. Plot made by INFN Trieste group.

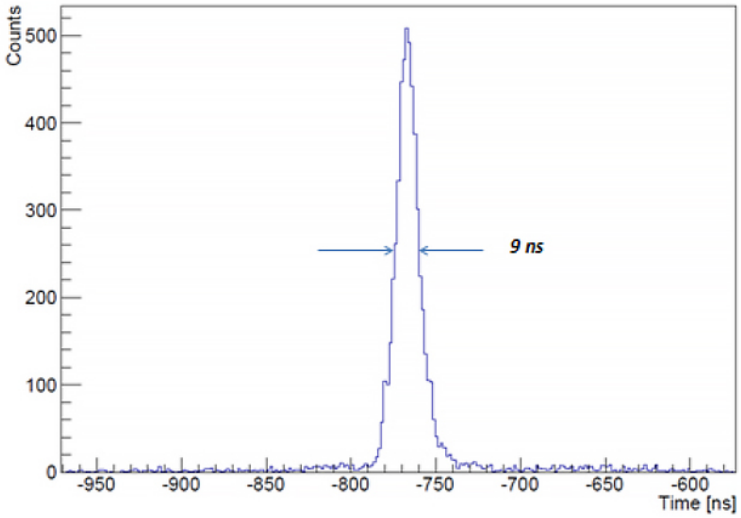

Figure 4.35: Time resolution of the prototype detectors[45]. Plot made by INFN Trieste group.

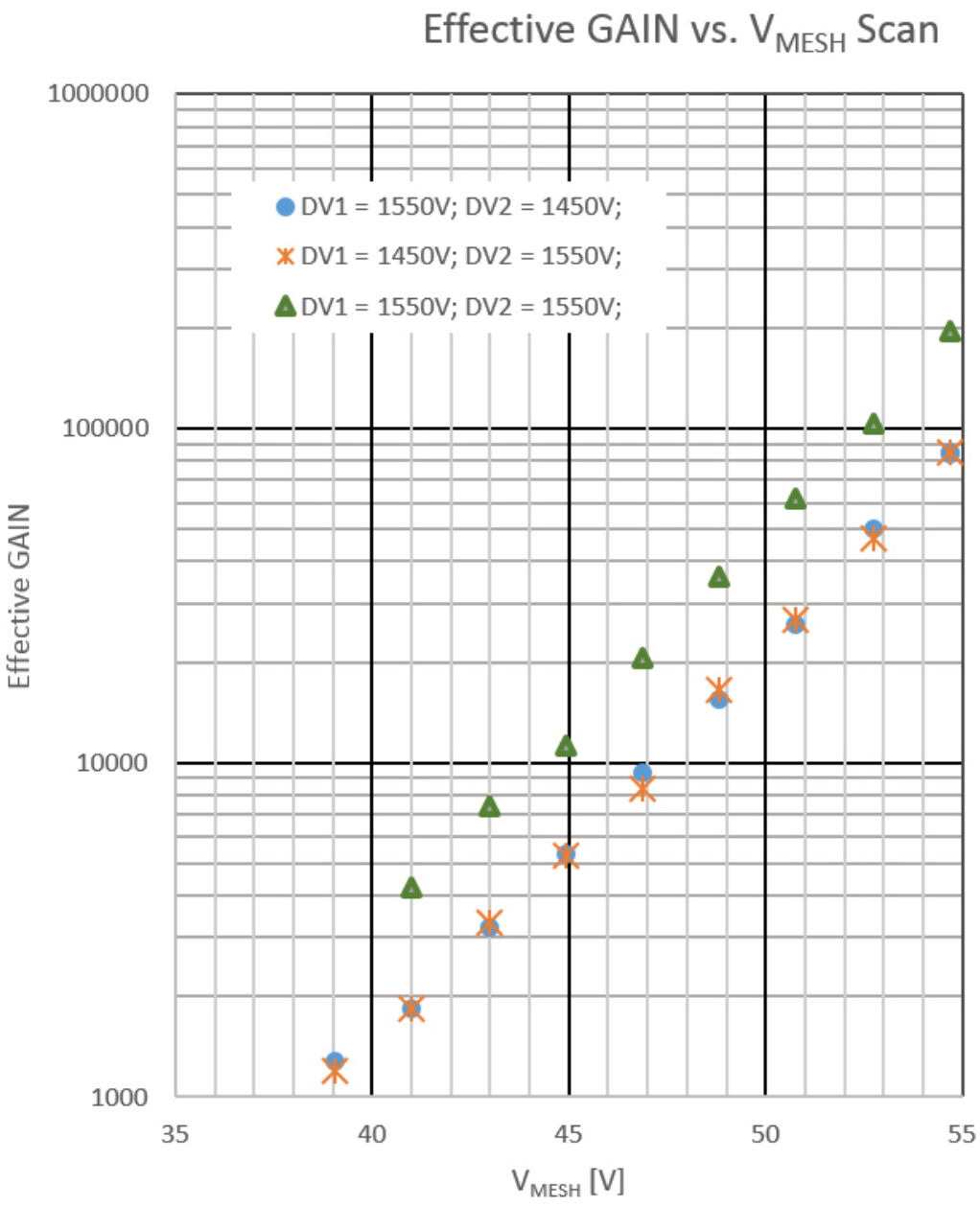

Figure 4.36: Dependency of the detector gain on the voltage applied to the micromesh. DV1 and DV2 mark the changing difference between the voltages between the top and the bottom side of the ThGEM1 and ThGEM2[45]. Plot made by INFN Trieste group.

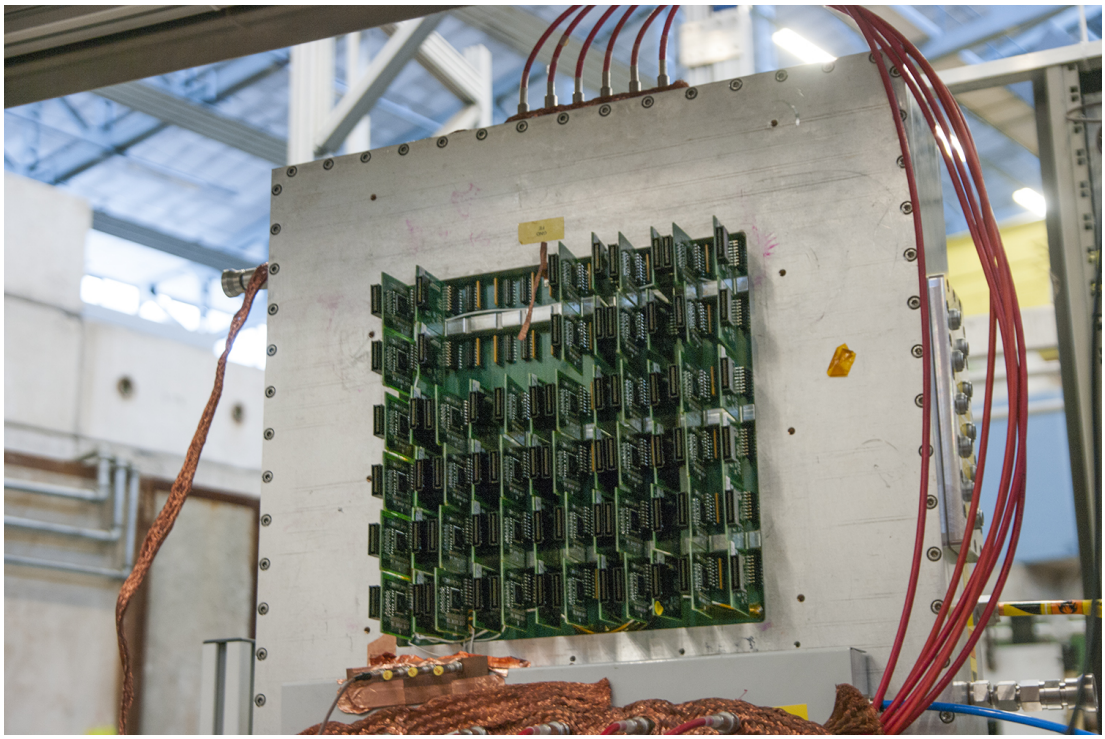

Figure 4.37: A prototype detector chamber with CMAD boards mounted.

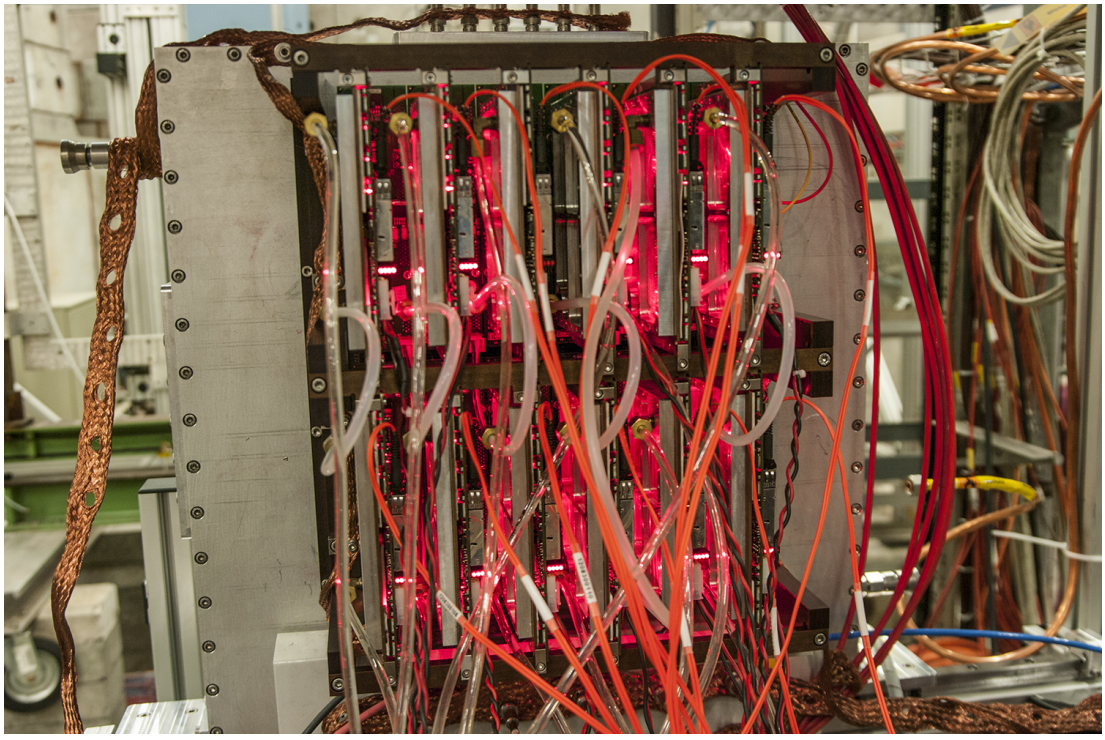

Figure 4.38: A prototype detector chamber with Digital RICH electronic sampling(DREISAM) boards mounted and activated. Notice the water cooling system of the boards and the optical uplink cables.

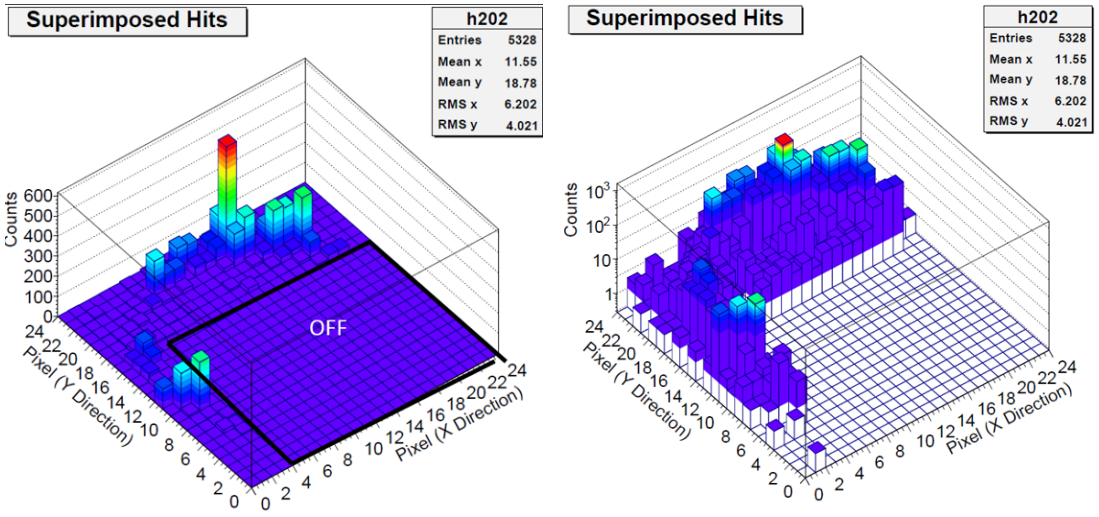

(a) (b)

Figure 4.39: A cherenkov ring image acquired using the digital readout system plotted using (a) linear scale, (b) logarithmic scale[45]. Plot made by INFN Torino group.

detector. These results also mean a progress from the 2012 test run, results of which have been presented in the chapter 4.3.2. The effective gain achieved in the detector is comparable, however the time resolution for the same gain levels is seemingly better.

The author of this thesis contributed in data taking, trigger set-up, automation attempts, overview spectra creation, chamber set-up in the Meyrin site, beam position finding, regular test condition checks and photo documentation of the test.

4.4.4 Digital readout measurement

The digital readout electronics used in the measurement were supplied to the test run by the Torino group. They are the same front-end readout electronics as the ones currently used on the RICH-1 reading out the MAPMTs. They comprise of the CMAD boards reading single readout sectors or "pixels"(a detector with CMADs mounted can be seen on figure 4.37) which are then interconnected by the ROOF boards, which supply the data for the water-cooled DREISAM boards(see figure 4.38), signals of which is read-out using an optical link. A detailed description of the boards and their function and implementation techniques can be found in [14].

However, reading-out these electronics proved a difficult task. A noise of an unknown origin has been present in the readout chain despite the robust grounding of the system rendering one big region of the detector unusable, allowing the measurement only with the region turned off. However, despite the difficulties and problems, an image of a Cherenkov ring was successfully obtained using only a portion of the detector. The resulting output can be seen on figure 4.39.

Despite the image being notably worse than what has been presented on the figure 4.17, the main focus of this measurement was to show that the detector is capable of imaging the cherenkov ring, which has been successfully done.

Detector:	**Big Sparky**	**Big Beauty**
Sector:	Trip count:	Trip count:
T11	159	152
T12	173	155
T13	182	160
T14	189	153
T15	140	144
T16	124	150
T21	151	154
T22	161	158
T23	171	155
T24	184	150
T25	126	150
T26	112	138
MESH	198	116
Total trips:	390	223

Table 4.1: Trip count for separate sectors for the both detectors. The T in the sector naming stands for the Top sector, the first number is the ThGEM number and the second is the sector number. We do not include the bottom plate sectors, since there was only one bottom plate sector for each ThGEM and an overcurrent of any top sector always triggered an overcurrent in the bottom sector. The detector sectoring can be seen on the figure 4.26.

4.4.5 Stability

Both detectors during the test run of August 2014 experienced a large number of discharges, or trips for short, between the ThGEM plates, ThGEM detectors, ThGEM and micromesh and between the micromesh and anodes. The drift region rarely experienced discharges because of its higher distance to the ThGEM plates. The discharge triggered an alert of overcurrent on some of the sectors in the GECO control software and the control software reacted to this situation by turning off the voltage supply to the sector slowly ramping up the voltage after each trip. All of the trips had a fast recovery time, almost always under one minute allowing for multiple trips occuring in one sector in one minute. Hence during a trip and the recovery period, the gain of the detector was reduced to zero, which can be seen from the figure 4.41, which shows the effect of the detector tripping to its gain.

From the recorded trips, a statistical file of 390 best-recorded trips has been chosen for the Big Sparky detector and a statistical file of 223 trips for the Big Beauty detector. The trip count for each detector by single sectors can be seen on table 4.1. From the table, we can see that for the Big Sparky the micromesh trips were most frequent and that the sectors 1-4 were predominant trippers. This is a very interesting fact, since the beam was directed to the sector 4. For the Big Beauty quite the contrary and the micromesh is the least-tripping sector and the ThGEM trip distribution is nearly constant throughout the both ThGEM detectors and their sectors.

The mean time between the trips has been calculated and reaches ($5.3177 \pm$

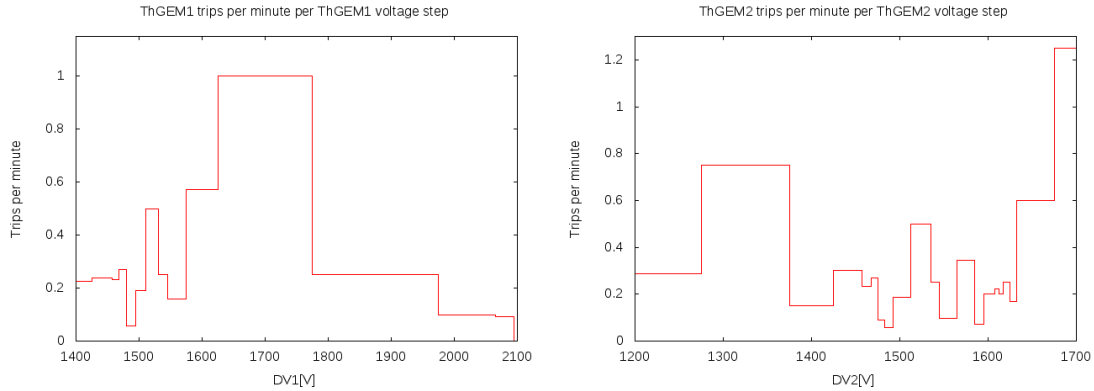

(a) ΔV_1 vs the trips per minute

(b) ΔV_2 vs the trips per minute

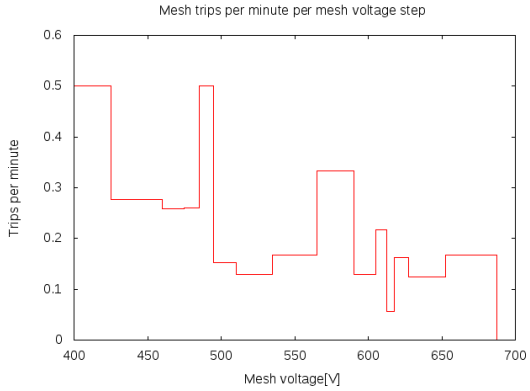

(c) V_{mesh} vs the trips per minute

Figure 4.40: Histograms showing the trip count voltage distribution of the statistical file for the Big Sparky detector. ΔV_1, or DV1 in the histogram, is the voltage difference between the top and the bottom plate of the ThGEM1, ΔV_2, or DV2 in the histogram, is the same for the ThGEM2 and the V_{mesh} is the voltage applied to the mesh.

0.0055)min for the Big Sparky detector and (7.221 ± 0.042)min for the Big Beauty detector. Based on the observation of multiple observers on the site of the experiment, the beam presence in the detector had no obvious short-term effect on the trip rate, however, some spills in fact induced the detector trips. Hence an experimental evidence would have to be collected to draw any conclusions.

The voltages during which the trips occurred for the Big Sparky detector were also recorded and can be seen in the table 4.2. These data are visualized on figure 4.40.

These data are interesting enough because the Big Sparky chamber was the longest-running chamber during the test run and various voltage scans were performed. The Big Beauty detector hasn't been tested with various voltages, almost all of the trips occurred when having the voltage difference on ThGEM1 $\Delta V_1 = 1300\,\text{V}$, for ThGEM2 $\Delta V_2 = 1500\,\text{V}$ and anode voltage of $\sim V_a = 600\,\text{V}$.

From the visualized data on figure 4.40 one can see that the trip distribution is rather random.

Even though the instability of the detector was rather high, the fast recovery time compared to the recovery time of the MWPCs discharges, that could reach

V_{mesh}[V]	TPM	ΔV_1[V]	TPM	ΔV_2[V]	TPM
400	0.5	1450	0.237	1350	0.75
450	0.277	1465	0.233	1400	0.15
470	0.259	1470	0.269	1450	0.303
480	0.261	1490	0.057	1465	0.233
490	0.5	1500	0.192	1470	0.269
500	0.152	1520	0.5	1480	0.091
520	0.129	1540	0.25	1485	0.057
550	0.167	1550	0.16	1500	0.187
580	0.333	1600	0.571	1525	0.5
600	0.13	1900	0.25	1540	0.25
610	0.217	2050	0.1	1550	0.098
615	0.057	2080	0.091	1580	0.345
620	0.163			1590	0.071
635	0.125			1600	0.2
670	0.167			1605	0.2
690	0.5			1610	0.222
1400	0.227			1200	0.286
1650	1			1530	0.5
				1615	0.2
				1620	0.25
				1630	0.167
				1635	0.6
				1650	0.6
				1700	1.25

Table 4.2: Trip distribution per voltage step for the Big Sparky detector chamber. ΔV_1 is the voltage difference between the top and the bottom plate of the ThGEM1, ΔV_2 is the voltage difference between the top and the bottom plate of the ThGEM2 and the V_{mesh} is the voltage applied to the mesh during which the trip occured. TPM means trips per minute.

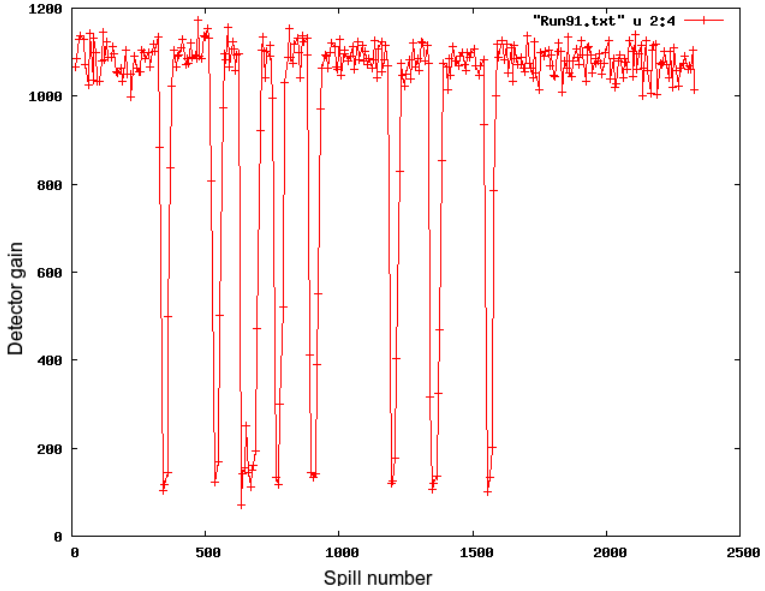

Figure 4.41: The effect of discharges on the detector gain for the single spills. The trips can be observed as an almost-instantaneous gain drops.

even 1 day long periods[44], allowed for a certain amount of automation of the data collection. However, trip rate of this value is not really acceptable for a sustainable long-term experiments and further research and development into the detector technology is needed to provide detectors of a higher stability.

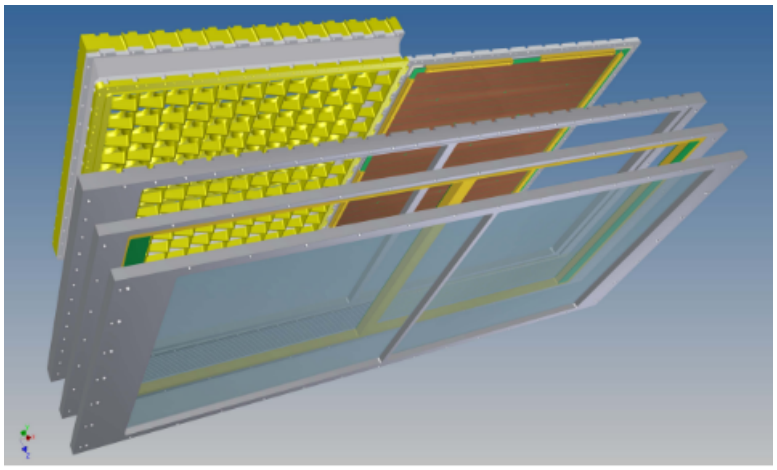

Figure 4.42: A 3D rendering of the exploded view of the foreseen structure of the upgraded COMPASS RICH-1 photon detector system[19]. On the left side of the detector we can see the telescopes of the MAPMTs and on the right side the ThGEM based detector system, the ThGEM detector covering the active area of $576 \times 576\,\mathrm{mm}^2$.

4.5 Upgrade of 2016

The main motive lying behind the tests with the novel ThGEM-based detector design provided in this chapter was the 2016 COMPASS RICH-1 detector upgrade, which sought to upgrade the currently used MWPCs in the outer detection region. The replacement of the MWPC cathodes has been done with a set of two groups of 6 ThGEM based detectors with the active area of $576 \times 576\,\mathrm{mm}^2$[19].

In the time of the tests, the $576 \times 576\,\mathrm{mm}^2$ ThGEM plates were already in production for further testing. The final photon detectors designed according presented tests has been already installed to COMPASS RICH-1 in the first quarter of the year 2016. It will be operational during the 2016 COMPASS data taking.

Conclusion

From the presented results of the test of hybrid photon detectors of 2014, it can be clearly seen that a progress has been made since the 2012 tests in the region of gain and time resolution.

By comparison, the ThGEMs presented in this thesis are capable of battling the LHCb Pixel HPDs and the MWPCs used on COMPASS RICH-1 and ALICE experiments in their performance in gain. They are not able to outperfom the MAPMTs used on COMPASS RICH-1, however, they are not meant to. They should rather complement the MAPMTs.

Even though the test run of 2014 was overflowing with difficulties, especially with the noise, the test run was a success. The stability of the detector, even though achieving results not reaching an applicable values for long-term use on a large-scale experiment, proved the flexibility and toughness of the novel hybrid photon detector design. However, despite the rather poor detector stability, the novel design proved itself to be superior to the MPWCs already used on COMPASS RICH-1 in the recovery time period. The novel detector's only a few-seconds long recovery time is considerably better than the one day long recovery time of the MPWCs. The detector also proved that it is capable of battling the already used MWPCs by its comparable gain.

The research on the geometrical parameters and practical features presented in the presented thesis and done during the test run are of an utmost importance for the future research and development of the hybrid photon detectors, their application in the Ring Imaging Cherenkov counters and had an impact on the decision on the final setup and design of the photon detectors replacing the MWPCs in the central region of COMPASS RICH-1 and will have an impact on the research and development of similar photon detectors in future experiments.

Bibliography

[1] CERN, [online]. Available at: http://home.web.cern.ch/about. Accessed: 2016-04-17.

[2] COMPASS, [online]. Available at: https://wwwcompass.cern.ch/. Accessed: 2016-04-17.

[3] The LHCb Detector, [online]. Available at: http://lhcb-public.web.cern.ch/lhcb-public/en/Detector/Detector-en.html. Accessed: 2016-04-19.

[4] Particle detectors at accelerators [online]. Available at: http://pdg.lbl.gov/2015/reviews/rpp2015-rev-particle-detectors-accel.pdf. Accessed 2016-06-24.

[5] Sir John Sealy Edward Townsend [online]. Available at: http://www.britannica.com/biography/John-Sealy-Edward-Townsend. Accessed 2016-06-24.

[6] The nobel prize in physics 1958 [online]. Available at: http://www.nobelprize.org/nobel_prizes/physics/laureates/1958/, 2014. Accesed 2016-06-24.

[7] Aamodt, K., et al. The ALICE experiment at the CERN LHC. *Journal of Instrumentation 3*, 08 (aug 2008), S08002.

[8] Abbon, P., et al. Fast Photon Detection for Particle Identification with COMPASS RICH-1. *Nucl. Instrum. Methods Phys. Res., A 580*, physics/0610066. 2 (Oct 2006), 906–909. 5 p.

[9] Abbon, P., et al. The COMPASS RICH-1 fast photon detection system. *Nuclear Instruments and Methods in Physics Research Section A: Accelerators, Spectrometers, Detectors and Associated Equipment 595* (sep 2008), 23–26.

[10] Abbon, P., et al. The COMPASS RICH-1 detector upgrade. *Eur. Phys. J. Spec. Top. 162* (2008), 251–257.

[11] Abbon, P., et al. The COMPASS RICH-1 fast photon detection system. *Nucl. Instrum. Methods Phys. Res., A 595*, 1 (2008), 23–26.

[12] Abbon, P., et al. Particle identification with COMPASS RICH-1. *Nuclear Instruments and Methods in Physics Research Section A: Accelerators, Spectrometers, Detectors and Associated Equipment 631* (dec 2010), 26–39.

[13] Abbon, P., et al. The experience of building and operating COMPASS RICH-1. *Nuclear Instruments and Methods in Physics Research Section A: Accelerators, Spectrometers, Detectors and Associated Equipment 639*, 1 (2011), 15 – 19. Proceedings of the Seventh International Workshop on Ring Imaging Cherenkov Detectors.

[14] Abbon, P., and Kolosov, V. N. Read-out electronics for fast photon detection with COMPASS RICH-1. *Nucl. Instrum. Methods Phys. Res., A 587*, 2-3 (2008), 371–387.

[15] Afanasiev, G. *Vavilov-Cherenkov and Synchrotron Radiation: Foundations and Applications*, first ed. Springer Science + Business Media, Inc., 2004.

[16] Aguilar-Benitez, M., et al. RING Imaging Cherenkov Detector (RICH) For the AMS Experiment. In *Proceedings, 30th International Cosmic Ray Conference (ICRC 2007)* (2007), vol. 2, pp. 461–464.

[17] Albrecht, E., et al. COMPASS RICH-1. *Nucl. Instrum. Methods Phys. Res., A 478*, 1-2 (2002), 340–3. Ninth International Vienna Conference on Instrumentation 2001, Vienna, Austria, 19-23 Feb. 2001. , In: Nuclear-Instruments-Methods-in-Physics-Research-Section-A (Accelerators, Spectrometers, Detectors and Associated Equipment) (Netherlands), vol.4.

[18] Albrecht, E., et al. The mirror system of COMPASS RICH-1. *Nucl. Instrum. Methods Phys. Res., A 502*, 1 (2003), 236–240.

[19] Alexeev, M., et al. Development of thgem-based photon detectors for cherenkov imaging counters. *Journal of Instrumentation 5*, 03 (2010), P03009.

[20] Alexeev, M., et al. Detection of single photons with thickgem-based counters. *Nuclear Instruments and Methods in Physics Research Section A: Accelerators, Spectrometers, Detectors and Associated Equipment 695* (2012), 159 – 162. New Developments in Photodetection {NDIP11}.

[21] Alexeev, M., et al. Development of THGEM-based Photon Detectors for COMPASS RICH-1. *Phys. Procedia 37* (2012), 781–788. 7 p.

[22] Alexeev, M., et al. Ion backflow in thick GEM-based detectors of single photons. *JINST 8* (2013), P01021.

[23] Alexeev, M., et al. Status and progress of the novel photon detectors based on THGEM and hybrid MPGD architectures. *Nucl. Instrum. Methods Phys. Res., A 766* (2014), 133–137. 5 p.

[24] Alexeev, M., et al. The gain in thick gem multipliers and its time-evolution. *Journal of Instrumentation 10*, 03 (2015), P03026.

[25] Cardinale, R. LHCB : The upgraded LHCb RICH detector: status and perspectives. May 2015.

[26] Cortizo, S. On dirac's delta calculus. Available at: `http://arxiv.org/pdf/funct-an/9510004v1.pdf`, 1995. Accessed 2016-04-23.

[27] Engelfried, J. Ring imaging cherenkov detectors. In *AIP Conference Proceedings* (2006), AIP, pp. 340–346.

[28] Faruqi, A. *Multi-wire proportional chambers*. North-Holland, 1977.

[29] Francke, T., and Peskov, V. *Innovative applications and developments of micro-pattern gaseous detectors*. IGI Global, 2014.

[30] Frank, I., and Tamm, I. Coherent visible radiation from fast electrons passing through matter. *CR Acad. Sci. USSR 14* (1937), 109–114.

[31] Gautheron, F., et al. COMPASS-II Proposal. Tech. Rep. CERN-SPSC-2010-014. SPSC-P-340, CERN, Geneva, May 2010.

[32] Hrubý, J. Čerenkovovo záření [online]. Available at: `http://www.pf.jcu.cz/stru/katedry/fyzika/prof/Svadlenkova/Cerenkovovo%20zareni.pdf`. Accessed 2016-04-18.

[33] Jackson, J. *Classical electrodynamics*, 3rd ed. Wiley, New York, c1999.

[34] Jahoda, K., and McCammon, D. Proportional counters as low energy photon detectors. *Nuclear Instruments and Methods in Physics Research Section A: Accelerators, Spectrometers, Detectors and Associated Equipment 272*, 3 (1988), 800 – 813.

[35] LHCb Collaboration. LHCb PID Upgrade Technical Design Report. Tech. Rep. CERN-LHCC-2013-022. LHCB-TDR-014, CERN, Geneva, Nov 2013. Accessed 2016-04-18.

[36] Matoušek, J. Studies of Drell-Yan process at Compass experiment. Master's thesis, Charles University in Prague, 2013.

[37] Pešek, M. Low temperature polarized target for spin structure studies of nucleons at COMPASS. Master's thesis, Charles University in Prague, 2014.

[38] Platchkov, S. Hadron structure studies with the COMPASS experiment at CERN[online]. Available at: `https://wwwcompass.cern.ch/compass/publications/talks/t2016/platchkov_HEPChile2016.pdf`. Accessed 2016-06-20.

[39] Procureur, S. Micromegas trackers for hadronic physics. *Modern Physics Letters A 28*, 13 (2013), 1340024.

[40] Roskot, M. Particle Identification using Ring Cherenkov Detector Technology at COMPASS Experiment. Master's thesis, Charles University of Prague, 2015.

[41] Schopferer, S. The gandalf high-resolution transient recorder system [online]. DPG Münster 2011, Available at: `http://hpfr03.physik.uni-freiburg.de/gandalf/modules/download_gallery/dl.php?file=36`. Accessed 2016-06-22.

[42] Skála, L. *Úvod do kvantové mechaniky*, 1st ed. Karolinum, Prague, 2011.

[43] Tamm, I. *Selected Papers*. Springer Berlin Heidelberg, Berlin, Heidelberg, 1991, ch. Radiation Emitted by Uniformly Moving Electrons, pp. 37–53.

[44] Tesarotto, F., et al. Long term experience and performance of COMPASS RICH-1. *J. Instrum. 9* (2014), C09011. 27 p.

[45] Tessarotto, F., and Levorato, S. NA58 RICH Test Beam T10 sept.2014 [online]. Available at: http://indico.cern.ch/event/313598/contributions/723910/subcontributions/57463/attachments/600283/826149/tessarotto_NA58_RICH_25_09_14.pdf. Accessed: 2016-06-26.

[46] Weisstein, E. W. Cosine integral. From MathWorld–A Wolfram Web Resource [online]. Available at: http://mathworld.wolfram.com//CosineIntegral.html. Accessed 2016-04-24.

[47] Weisstein, E. W. Exponential integral. From MathWorld–A Wolfram Web Resource [online]. Available at: http://mathworld.wolfram.com/ExponentialIntegral.html. Accessed 2016-04-24.

[48] Weisstein, E. W. Sine integral. From MathWorld–A Wolfram Web Resource [online]. Available at: http://mathworld.wolfram.com//SineIntegral.html. Accessed 2016-04-24.

[49] Wheeler, N. Simplified production of dirac delta function identities [online]. Available at: http://www.reed.edu/physics/faculty/wheeler/documents/Miscellaneous%20Math/Delta%20Functions/Simplified%20Dirac%20Delta.pdf, nov 1997. Accessed 2016-04-25.

List of Figures

List of Tables

List of Abbreviations

ALICE - A large ion collider experiment

AMS - Alpha magnetic spectrometer

CERN - Centre Européne pour la Recherché Nucleaire

CLAM - Continuous Line Alignment Monitoring

COMPASS - Common muon proton apparatus for structure and spectroscopy

DIRC - Detection of internally reflected Cherenkov light

DREISAM - Digital RICH electronic sampling

GANDALF - Generic Advanced Numerical Device for Analog and Logic Functions

HMPID - High momentum particle identification detector

HPD - Hybrid Photon Detector

HV - High voltage

INFN - Instituto Nazionale di Fisica Nucleare

ISS - International space station

LHCb - Large hadron collider beauty

MAPMT - Multi-anode photomultiplier

MIPS - Minimum Ionizing Particles

MWPC - Multi-wire proportional chamber

NIM - Nuclear instrumentation module

PCB - Printed circuit board

PID - Particle identification

QCD - Quantum chromodynamics

RICH - Ring imaging Cherenkov

SLAC - Stanford linear accelerator center

SPS - Super Proton Synchrotron

TPM - Trips per minute

TTL - Transistor-transistor logic

VC - Vavilov-Cherenkov